

1 **Title:** *Detection of cropland field parcels from Landsat imagery*

2 **Authors:** Jordan Graesser^{a,*}, Navin Ramankutty^b

3 **Author details:**

4 ^a Department of Geography, McGill University, Montreal, QC H3A2K6, Canada

5 ^b The Liu Institute for Global Issues and Institute for Resources, Environment, and Sustainability,
6 University of British Columbia, 6476 NW Marine Drive, Vancouver, BC V6T1Z2 Canada

7 **Role of authors:** JG contributed to ideas, work, writing, and stewardship, with an overall
8 estimated contribution of 80%. NR contributed to ideas, work, writing, and stewardship, with
9 an overall estimated contribution of 20%.

10 **Conflict of interest:** The authors declare no conflict of interest.

11 **Role of the funding source:** The funding source had no involvement in the research.

12
13 *corresponding author

14 *Email: graesser@bu.edu

15 *Permanent address: 60 Otis St., Apt. 1, Cambridge, MA, USA, 02141

<https://doi.org/10.1016/j.rse.2017.08.027>

Graesser, J., & Ramankutty, N. (2017). Detection of cropland field parcels from Landsat imagery. *Remote sensing of environment*, 201, 165-180.

Abstract

A slowdown in global agricultural expansion, spurred by land limitations, improved technologies, and demand for specific crops has led to increased agricultural intensification. While agricultural expansion has been heavily scrutinized, less attention has been paid to changes within cropland systems. Here we present a method to detect individual cropland field parcels from temporal Landsat imagery to improve cropland estimates and better depict the scale of farming across South America. The methods consist of multi-spectral image edge extraction and multi-scale contrast limited adaptive histogram equalization (CLAHE) and adaptive thresholding using Landsat Surface Reflectance Climate Data Record (CDR) products. We tested our methods across a South American region with approximately 82% of the 2000/2001 total cropland area, using a Landsat time series composite with a January 1, 2000 to August 1, 2001 timeframe. A thematic accuracy assessment revealed an overall cropland f-score of 91%, while an object-based assessment of 5,480 fields showed low geometric errors. The results illustrate that Landsat time series can be used to accurately estimate cropland in South America, and the low geometric errors of the per-parcel estimates highlight the applicability of the proposed methods over a large area. Our approach offers a new technique of analyzing agricultural changes across a broad geographic scale. By using multi-temporal Landsat imagery with a semi-automatic field extraction approach, we can monitor within-agricultural changes at a high degree of accuracy, and advance our understanding of regional agricultural expansion and intensification dynamics across South America.

Keywords: cropland, field, Landsat, South America

1. Introduction

In the latter half of the 20th century, growing food demand was met through intensification of agricultural production, while global agricultural expansion slowed down (Tilman et al., 2001). Farmers raised productivity through increased application of inputs such as fertilizers, herbicides, and pesticides, and by adopting modern plant varieties, mechanization, and new farming techniques (Deininger & Byerlee, 2012; Matson et al., 1997). While reduced land clearing for agriculture (Gibbs et al., 2010; Gibbs et al., 2015; Graesser et al., 2015) can contribute greatly to biodiversity preservation and habitat conservation (Foley et al., 2005), intensification can be environmentally harmful when inputs such as nitrogen and phosphorous are mismanaged (Barrett et al, 2001; Tilman et al., 2001; Tilman et al., 2002). Thus, there is a critical need for agricultural monitoring to assess the environmental implications of agro-industrialization and intensification.

Timely and consistent monitoring of agricultural intensification is challenging because the availability of data that describe intensification over large areas is limited. For example, agricultural censuses provide information about farm size, machinery, and fertilizers, but these data lack the spatial and temporal resolution needed to consistently monitor detailed changes over large areas. Remote sensing, however, offers a unique solution to this problem. Remote sensing provides the capability to detect indicators of intensification, namely indicators of physical agricultural characteristics. For example, agricultural morphology, i.e., field shape or size, is observable with moderate- to high-resolution sensors, and would be an invaluable piece of information for multiple reasons. Field size is important in order to understand farm management practices such as crop diversity and rotation, and to assess tradeoffs between

agricultural scale and efficiency, biodiversity monitoring, landscape fragmentation, and ecological diversity (Barrett et al., 2001; Fahrig et al., 2015). Field size is also complementary to farm size. For example, if a farmer's capacity to expand land holdings is limited, farm size remains unchanged. But a farmer can still alter the landscape through changes in management such as field enlargement. Therefore, field size can provide important information about the planet's rapidly changing agricultural systems that would not otherwise be captured with farm size data from agricultural censuses and surveys. Fortunately, Landsat, one of the remote sensing community's long-standing pillars of global change monitoring, offers the geographic and temporal coverage as well as the spatial resolution necessary to detect cropland field parcels over large areas. The challenge is to exploit this vast resource and design practical and robust methods to accurately depict field parcels, which will complement growing information about agricultural expansion.

While the remote sensing community has remarkably improved the capacity to monitor extensive land cover changes, particularly into forests (Hansen et al., 2008; Hansen et al., 2012; Potapov et al., 2012), less has been accomplished to remotely depict land use intensification such as field size changes. Part of the challenge is that traditional per-pixel based methods are not suitable for understanding landscape shape and context. Instead, image processing methods are essential to solving this problem. For example, contextual information, often referred to as image texture, can provide useful information about the structure and morphology of landscape context. This approach was used in combination with linear regression to estimate field sizes at a continuous scale in Eastern Europe (Kuemmerle et al., 2009). Though computationally simple and shown to produce accurate estimates, the method

restricts the data output to large area units rather than individual field parcels. Similar to this work, European-wide field size estimates were conducted from interpolation of survey data (Kuemmerle et al., 2013). A very different approach from the previous studies made use of crowdsourcing to rapidly produce many field size samples from satellite imagery (Fritz et al., 2015). By doing so, the authors produced, to our knowledge, the first and only global estimate of field sizes, offering a first look at the major global patterns on the scale of food production. However, the methodology does not provide wall-to-wall estimates, instead interpolating between crowdsourced samples. Although somewhat expected in global studies, the result is an over-generalization of field sizes because of categorical field size classes and assumptions about field size patterns over interpolated space. Still, Argentina—particularly scrutinized because of our paper’s regional focus—is a case in point of the limitations of this approach. Only remnants of small fields (although ‘small’ is not explicitly defined) were estimated, when in fact many small fields exist throughout the country, as we shall show later.

The limitations (reliance on third-party data, coarse field estimates) of the approaches above warrant a solution that can produce wall-to-wall, large-scale estimates of individual fields. Yan and Roy (2014) developed a novel procedure to detect individual parcels from multi-temporal Landsat imagery by combining image-processing techniques such as image morphology and segmentation. The authors employed temporal Web-enabled Landsat Data (WELD) (Roy et al., 2010) to extract fields over a five-year period in the United States and presented the first large-scale estimate of individual fields. More recently, the authors reduced the timeframe to one year, refined the methods, and applied their algorithm to the contiguous US (Yan and Roy, 2016). Their approach, utilizing a combination of image processing methods, is

more promising than previous approaches. Another European-wide study illustrated the potential for 'field patch' segmentation from satellite imagery (Weissteiner et al., 2016). However, whereas the estimates of Yan and Roy (2016) were kept at the field level, Weissteiner et al. (2016) aggregated their data to a much coarser scale than individual fields.

In this study, we present an image processing method to detect individual field parcels from multi-temporal Landsat imagery, with some key differences from the Yan and Roy studies, and with application over different agricultural landscapes across much of South America. South America's agricultural landscape has changed rapidly over the past several decades (Berdegué and Fuentealba, 2011; Dros, 2004; FAO, 2015; Graesser et al., 2015; Martinelli, 2012). Better estimates of cropland and data that describe the nature of the agricultural changes are needed in order to accurately monitor and understand the consequences of these rapid changes. Field-size data, in particular, would greatly enhance the capacity to monitor the scale of these changes. This study addresses two questions: 1) Is Landsat a reliable sensor for cropland observations? and 2) Can individual field parcels be detected at the continental scale from multi-temporal Landsat imagery over a broad range of crop types and field configurations? To characterize cropland, we used all available Landsat scenes over a 1.5-year period, from 2000 to 2001. We then estimated cropland at a parcel level using multi-temporal Landsat imagery and contemporary edge-based methods, and tested the robustness of our methods over a large and complex agricultural region of South America.

2. Data and study area

2.1 Study area

We identified individual crop field parcels across a selected region of South America, broadly defined as cropland south of the Amazon River and north of Patagonia (Fig. 1). The test region was chosen from Landsat scenes that intersected selected world ecoregions (Olson et al., 2001) in order to include a wide range of crop types and landscapes. This selected region contained approximately 82% of the 2001 South American cropland area (Graesser et al., 2015). Argentina and Brazil comprise the majority of the agricultural land within the study region. Bolivia, Paraguay, and Uruguay have substantially less agricultural land, but are important agricultural economies. Chile's agricultural landscape is perhaps the most diverse, with a wide range of small, specialized production, to large-scale grain production. Of the countries included, only Argentina, Paraguay, and Uruguay are completely within the study boundary. In contrast, the area included of Bolivia, Brazil, and Chile generally comprises land outside of the Amazon and Andes regions, but still includes a large portion of the respective country's agricultural area.

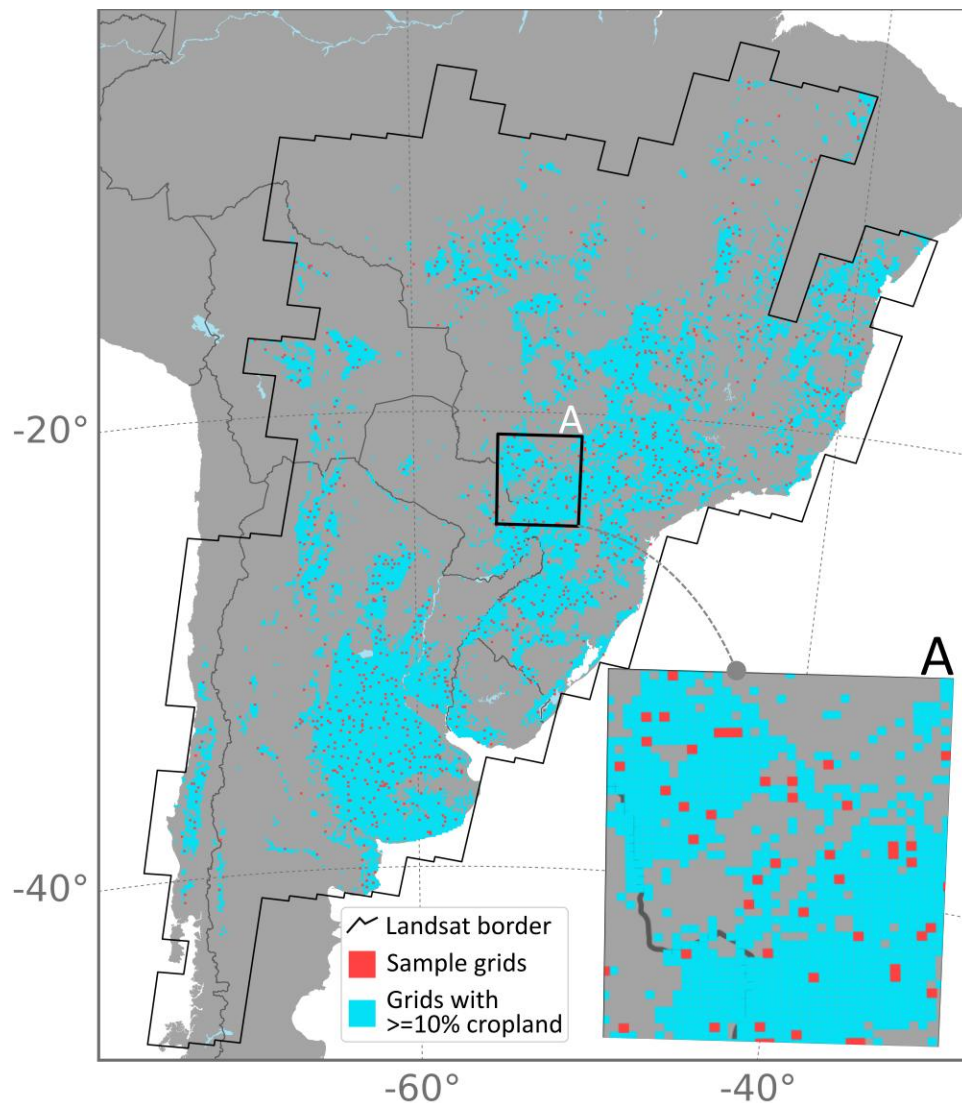


Figure 1. South America test region for semi-automatic crop-field extraction. The study area (shown in black outline) consists of Landsat scenes that intersect selected ecoregions. For field parcel validation, 10 km x 10 km grids were generated to cover the test region. The grids were then restricted to those with $\geq 10\%$ cropland area (shown in cyan). Finally, we randomly sampled 1,000 grids (shown in red) from this $\geq 10\%$ cropland grid to use for crop field parcel validation. Inset **A** illustrates a larger-scale view of the sample grids.

2.2 Data and timeframe

The Landsat Surface Reflectance Climate Data Record (CDR) product is freely available by request through the U.S. Geological Survey (USGS) Earth Resources Observation and Science

Center (EROS) Science Processing Architecture (ESPA) (<http://espa.cr.usgs.gov>). The USGS creates the CDR product by converting Landsat data to surface reflectance using the 6S radiative transfer model (Vermote et al., 1997). We acquired all Landsat 5 Thematic Mapper (TM) and Landsat 7 Enhanced Thematic Mapper Plus (ETM+) CDR scenes over the study area for the 2000/2001 season that had 70% or less cloud cover. The temporal range of the coverage is January 1, 2000 to August 1, 2001 and captures one full cycle of the agricultural growing season in the study area. Each image comprises 6 reflective bands (1-5 and 7, specifically the blue (0.45—0.52 μm), green (0.53—0.61 μm), red (0.63—0.69 μm), near-infrared (0.76—0.9 μm), and mid-infrared (1.55—1.75 μm and 2.08—2.35 μm) wavelengths) and the Fmask atmospheric mask with cloud, water, and shadow flags (Zhu & Woodcock, 2012).

Our objective in this study was to test the field extraction methods over a large geographic space. We could have chosen any timeframe to apply the methods. We used imagery from 2000 and 2001 because there was a plentiful supply of Landsat data and it roughly represents the starting point from which agriculture began to expand rapidly in South America (FAO 2015).

3. Methods

The proposed methodology uses Landsat satellite time-series composites to detect crop field parcels over an agricultural growing season, using a semi-automatic approach. The generalized workflow is shown in Figure 2 and broadly defined as: 1) image time-series computation over one agricultural growing season; 2) multi-scale contrast limited adaptive histogram equalization (CLAHE) and adaptive thresholding (ATh); 3) morphological edge cleaning; and 4) delineation of

individual cropland field parcels. The details are described in the following sub-sections and explain the semi-automatic procedure to extract land-cover object edges and label individual crop fields.

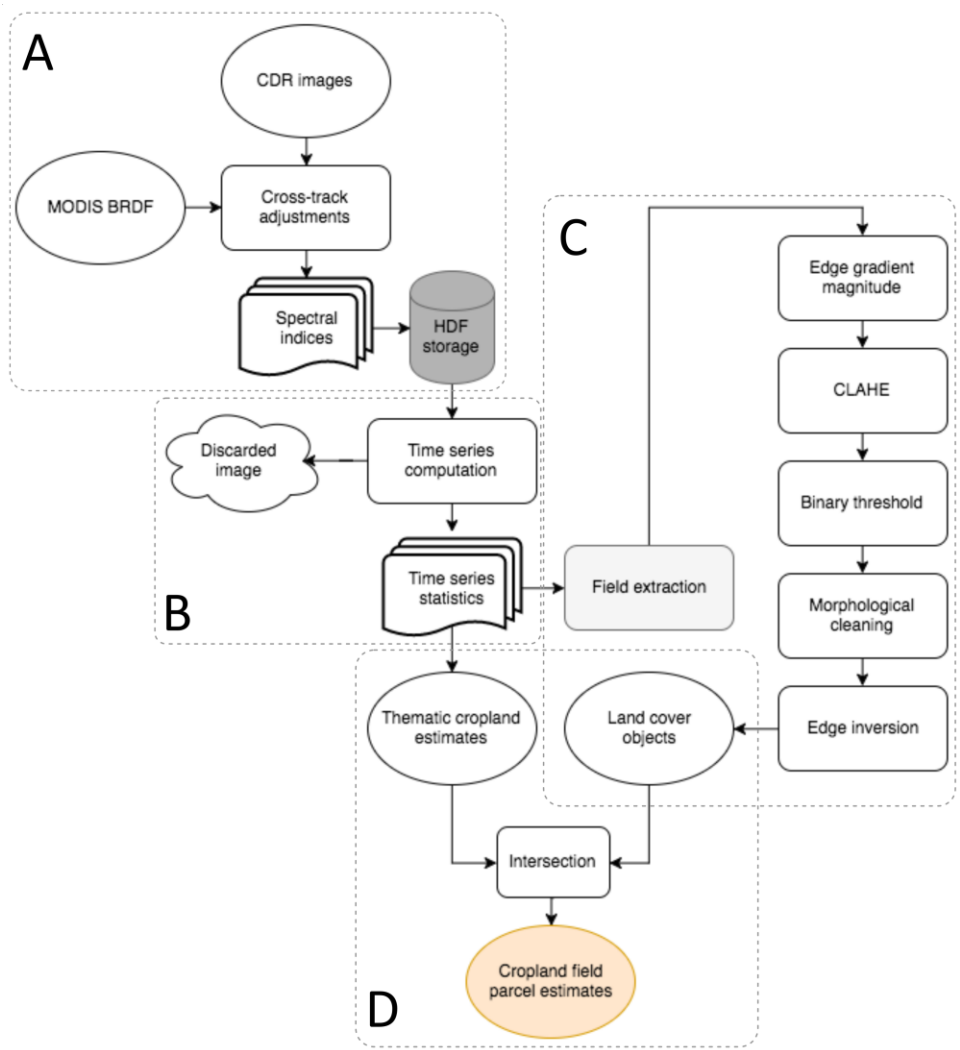


Figure 2. The general workflow of Landsat processing, cropland classification, and cropland field parcel detection, with the main components: A) Landsat pre-processing; B) time-series computation; C) land-cover object extraction; and D) cropland and field parcel intersection.

3.1 Field definition

None of the literature reviewed clearly defined an agricultural field. The definition of a crop field may vary by disciplines and research questions. For some, a field may represent land tenure, which is related to rules of property rights allocation rather than how the plot of land is managed. But tenure is more closely associated to farm size rather than field size. Here we defined fields as representing individual crops planted throughout a year (Fig. 3). In Figure 3 we illustrate one plot of land under the same ownership over one year, with three crops planted during the first phase of the rotation and two crops planted during the second, with a double crop of soy replacing wheat. Although the land tenure did not change during the year, the type and number of crops did. The objective of this study is to identify the highest parcel-level resolution at which crops were cultivated during a growing season, illustrated by the three crops in the first half of the rotation.

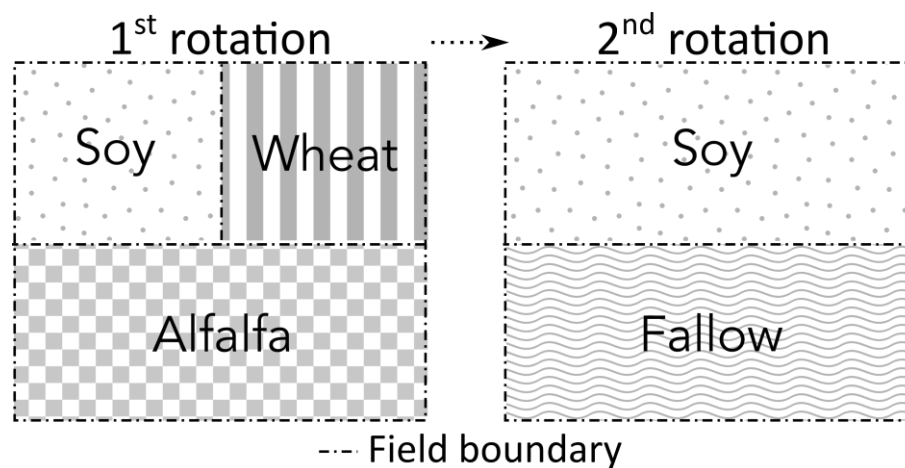


Figure 3. Illustrative diagram of field sizes under one tenure system. The left panel displays three crops that were grown during the first phase of the crop rotation. The following rotation phase brought a double crop of soybeans (wheat to soybean rotation). This study considers the highest field resolution of cultivated crops throughout the example season to be 3.

3.2 *Landsat pre-processing*

Prior to field extraction, we processed Landsat imagery in the following steps: 1) climate surface reflectance (CDR) imagery were acquired from USGS; and for each scene we 2) normalized cross-track surface reflectance variations; 3) computed spectral indices; and 4) computed temporal descriptive statistics from step 3.

3.2.1 *Radiometric adjustments*

Radiometric normalization is desirable to remove scene-to-scene variations and allow for standardized land cover sampling across scenes. Atmospheric conditions and surface inconsistencies impede image normalization and standard classification models, particularly over large areas. Thus, radiometric adjustments are necessary to account for varying atmospheric conditions (Flood et al., 2013). The 6S radiative transfer model, used to produce the CDR product, converts Landsat data to atmospherically corrected surface reflectance. However, the CDR products are not corrected for cross-track degradation, an issue observed in Landsat imagery (Hansen and Loveland, 2012; Toivonen et al., 2006), and observed in the bulk of the scenes covering our study region. We used the MODerate-resolution Imaging Spectroradiometer (MODIS) bidirectional distribution function (BRDF) satellite product (MCD43A4) to normalize the CDR cross-track spectral response. First, for each pixel we computed the two-year (2000 and 2001) median of the MODIS BRDF MCD43A4 product (hereafter, referred to as MODMED). Following methods similar to Gao et al. (2011) and Potapov et al. (2012), we fit robust linear functions of each individual CDR band against the matching MODMED wavelength. Each Landsat band was downsampled to 500 m to match the

215 spatial resolution of the MODMED composites. Then the Landsat values were subtracted from
216 MODMED (MODMED minus Landsat reflectance bias) for each MODMED-Landsat paired band.
217 Starting in the western scan edge all values within a 40 km-wide (i.e., 0 km to 40 km from scene
218 edge) column were extracted. Any cloud or shadow pixels in the CDR Fmask, or poor-quality
219 pixels in the MODIS MCD43A2 quality layer, were removed. We then used the mean of the
220 remaining MODMED-Landsat bias pixels. The mean column bias (y) and the distance (km) from
221 the western scene edge to the column center (x) were recorded. The next 40 km-wide column
222 was selected by moving the column selection 20 km east of the current scan column, creating
223 columns with 20 km overlaps. This process was repeated until the eastern scene edge was
224 reached. Lastly, the set of bias values (y) and distance to column centers (x) were regressed
225 with a Theil Sen linear regression (Theil, 1992). As mentioned, we used the CDR Fmask and
226 MODIS MCD43A2 quality products to mask “bad” pixels. However, the Theil Sen model was
227 used in order to address any misclassifications (extreme outliers) in the mask products. Finally,
228 the predicted bias was applied to the original 30 m CDR band to create the final adjusted band.
229 An illustration of the procedure is shown in Figure 4. Scenes where we could not extract
230 sufficient cross-track column samples were adjusted using a linear function of all clear
231 MODMED pixels (x_s) to estimate CDR surface reflectance (y_s) (i.e., $y_s = ax_s + b$, with no cross-
232 track adjustments). The cross-track method improved the scene-to-scene normalization after
233 visually comparing the results to the CDR bands (i.e., with no cross-track adjustments) for the
234 study region.

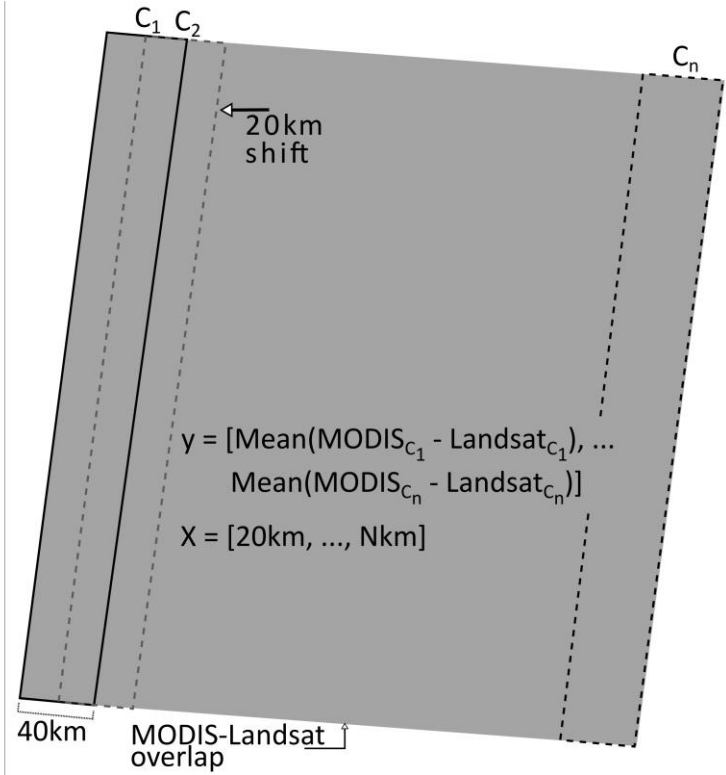


Figure 4. Landsat cross-track adjustment using the 500 m MODIS Bidirectional Reflectance Distribution Function product-derived MODMED. Starting at the western scene edge, Landsat and MODMED pixel values are extracted from a CW km-wide column ($CW=40$). After removing atmospherically contaminated pixels, the mean of the remaining column (C_1) pixels is computed and stored in the y vector. For the X vector, the distance from the scene edge to the center of C_1 is recorded. The column is then shifted half the width of CW (20 km), overlapping the first column, and the process is repeated until the eastern scene edge is reached. The y and X vectors are used to normalize the image.

3.2.2 Spectral transformations

The timing of crop planting and harvesting can vary from field to field and over large regions. Therefore, we used multiple spectral transformations to exploit the complete spectrum of different crops. We used descriptive statistics computed from temporal composites of spectral

indices—instead of the CDR spectral bands—for image edge extraction and classification. Initially, we computed five vegetation spectral indices from each CDR image: the normalized difference vegetation index (NDVI), the enhanced vegetation index (EVI2), the green normalized difference vegetation index (GNDVI), the normalized difference soil index (NDSI), and the normalized difference bareness index (NDBaI) (Table 1). Each spectral index image array and its image information were stored in a HDF5 (Hierarchical Data Format) database (Alted & Vilata, 2002--) for efficient storage and fast query indexing.

Table 1. Spectral vegetation transformations.

Vegetation Index	Equation	Reference
NDVI	$(NIR - red) / (NIR + red)$	Tucker, 1979
EVI2	$2.5 * \left[\frac{(NIR - red)}{(NIR + (2.4 * red) + 1)} \right]$	Jiang et al., 2008
NDSI	$(MidIR - NIR) / (MidIR + NIR)$	Rogers & Kearney, 2004
NDBaI	$(FarIR - NIR) / (FarIR + NIR)$	Zhao & Chen, 2005
GNDVI	$(NIR - green) / (NIR + green)$	Gitelson et al., 1996

3.2.3 Time series composites

Seasonal satellite composites are necessary to accurately estimate row-crop agriculture because cropland typically produces a unique spectral response if measured over an entire growing season. Landsat time series compositing methods have become more commonplace since the opening of the Landsat archive in 2008 (Woodcock et al., 2008), which allowed researchers to develop composite datasets at a higher spatial resolution than previously

possible. Compositing methods range from the selection of single statistics over a year or multi-year timespan (Maxwell and Sylvester, 2012; Yan and Roy, 2014; Yan and Roy, 2016), ‘best available pixel’ selection based on probability scoring functions over several years (Griffiths et al., 2013; White et al., 2014), spatial and temporal gap-free (proxy value) composites (Hermosilla et al., 2015), atmospheric coverage rules (Roy et al., 2010), preferential seasonal selection (Potapov et al., 2012), synthetic time series generation (Schmidt et al., 2016), and descriptive statistics of spectral indices and transformations from an image time series (Gebhardt et al., 2014). Regardless of the compositing technique, pixel-based compositing offers advantages over previous scene-based approaches, particularly by the inclusion of (potentially) thousands of cloud-free samples that were otherwise excluded in scene-based criteria. In this study, we used pixel-based compositing to produce radiometrically consistent data across the study region. The composites were then used to estimate cropland and extract individual field parcels across the study area.

To compute a time series composite for a single Landsat path/row, we automatically checked each image in the path/row for: 1) extents larger than two standard deviations from the path/row mean extent size (indicating large image shifts); and 2) images with valid data (i.e., non-background) totals smaller than two standard deviations from the path/row mean valid data count. If any of the two checks were true, then the image was discarded from further use. A third, visual, check was performed to identify mis-registered images (pixel shifts as opposed to large image offsets) post time-series compositing, and automatically adjusted using cross-correlation (Guizar-Sicairos et al., 2008). If a path/row time-series composite was found to contain a mis-registered image, we cross-checked the mis-registered image in the path/row

for alignment against the nearest Julian day reference image with sufficient clear observations, and recorded the x and y coordinate shifts (derived from the cross-correlation procedure) against the nearest reference image. The x and y coordinate shift was inverted to apply the shift adjustment. To limit atmospheric contamination in the cross-correlation process, test and reference images were scanned for clear image blocks. The image was scanned for blocks with 99% clear data, starting with the largest square block that fit an image's valid data area. The block size was reduced by 64 pixels on each side and the image was re-scanned until an uncontaminated block was found. The final set of images for the path/row was then used for time series calculations.

Next, the images were sorted by year and Julian day, and cloud and shadow pixels were flagged using the CDR Fmask at each acquisition date. Missing observations in each spectral transformation were interpolated using the flagged pixels and linear interpolation following:

$$T_{i,j} = \frac{(x_2 - x_1) * (y_3 - y_1)}{(x_3 - x_1)} + y_1 \quad (1)$$

where, x_1 and x_3 are index positions around the position to be interpolated, x_2 , and y_1 and y_3 are the values around the day to be interpolated, $T_{i,j}$, at pixel location i, j . After interpolation, we applied a second order Savitsky-Golay filter (Savitsky & Golay, 1964) to smooth the time series at each pixel. We then computed 10 time-series statistics, namely the minimum, maximum, mean, coefficient of variation (CV), 25th, 50th, and 75th percentiles, maximum slope, minimum slope, and day of maximum value. The maximum and minimum slopes were computed with a moving window ($n=7$). The resulting set of variables was:

$$S_i = \{NDVI_i^{10}, EVI2_i^{10}, GNDVI_i^{10}, NDSI_i^{10}, NDBaI_i^{10}\}$$

where, S_I is the set of annual statistics for image I , and the superscript denotes the number of time series statistics computed. Thus, there were fifty statistical layers for each path/row time series.

3.3 Edge and object extraction overview

The large range of field sizes in South America prevents the use of global thresholds on dense concentrations of small fields (generally less than 2 ha), particularly at the Landsat spatial scale of 30 m. Here, small field size is relative to the study region, where farm and field sizes are larger than what is found in regions such as sub-Saharan Africa and South and Southeast Asia. High global edge-thresholds that appeal to large fields with strong edges tend to under-segment small, dense field clusters. Alternatively, lower edge-thresholds that address dense regions with very small fields over-segment large fields. Our solution was to apply a series of multi-directional convolution kernels to extract the edge gradient magnitude (EGM) from selected S_I variables (explained in detail in section 3.3.1), and then use multi-scale contrast limited adaptive histogram equalization (CLAHE) and adaptive thresholding (ATh), followed by image morphology to extract land cover object edges. The multi-scale approach reduced the threshold bias that might occur with one window size. Image edges were subsequently “cleaned” with image morphology, where edges were morphologically thinned and edge ends linked to close small gaps. Finally, detected object edges were intersected with thematic cropland estimates (procedure described in section 3.4) to predict individual cropland field parcels. The following sub-sections describe the edge extraction methods in detail.

3.3.1 Edge extraction

A subset of S_I was required for field extraction, because whereas a machine learning approach can ‘learn’ to set aside noisy data, our object segmentation approach uses all input data given. The set of variables used for field extraction is given as:

$$SSUB_I = \{NDVI_I^4, EVI2_I^4, GNDVI_I^4, NDSI_I^4, NDBaI_I^4\}$$

where the new superscript denotes the 50th, 75th, and 95th percentile variables, and the CV, and excludes the remaining 6 time-series statistics. After visual analysis, this subset of time series statistics provided the most consistent set of variables that were least affected by cloud mask errors. Prior to edge extraction, each $SSUB_I$ variable was smoothed using a bilateral filter (Tomasi & Manduchi, 1998). A bilateral filter is a weighted average of local pixels but, importantly, considers pixel neighbors in the color *and* spatial domain. This has the effect of smoothing image noise while preserving true edges. Next, we applied a series of x, y convolution kernels to extract the normalized EGM (dynamic range of 0-1) from $SSUB_I$. Image convolution is the sum of the local product of a kernel pair (k) (Fig. 5) and an image.

$$\begin{aligned} (1) & \begin{bmatrix} 0 & -1 & 0 & 1 \\ 1 & 0 & -1 & 0 \end{bmatrix} & (2) & \begin{bmatrix} -1 & 0 & 1 & 0 \\ 0 & 1 & 0 & -1 \end{bmatrix} & (3) & \begin{bmatrix} 1 & 1 & 1 & -1 & -1 & -1 \\ 0 & 0 & 0 & 0 & 0 & 0 \\ -1 & -1 & -1 & 1 & 1 & 1 \end{bmatrix} & (4) & \begin{bmatrix} 1 & 0 & -1 & -1 & 0 & 1 \\ 1 & 0 & -1 & -1 & 0 & 1 \\ 1 & 0 & -1 & -1 & 0 & 1 \end{bmatrix} \\ (5) & \begin{bmatrix} -1 & -1 & 1 & 1 \\ 1 & 1 & -1 & -1 \end{bmatrix} & (6) & \begin{bmatrix} -1 & 1 & 1 & -1 \\ -1 & 1 & 1 & -1 \end{bmatrix} & (7) & \begin{bmatrix} 1 & 1 & 0 & -1 & -1 & 0 \\ 1 & 0 & -1 & -1 & 0 & 1 \\ 0 & -1 & -1 & 0 & 1 & 1 \end{bmatrix} & (8) & \begin{bmatrix} 0 & -1 & -1 & 0 & 1 & 1 \\ 1 & 0 & -1 & -1 & 0 & 1 \\ 1 & 1 & 0 & -1 & -1 & 0 \end{bmatrix} \end{aligned}$$

Figure 5. Pre-defined convolution kernel pairs. Each bracket consists of a x, y symmetric kernel pair used to detect object edges.

345 The pairs are reflections of each other, so we computed a set of EGM images by image
 346 convolution as:

347

$$SSUB_I^V EGM_{i,j} = \sum_{ts \in 1,2,3,4} \left[\max_{mean} \left\{ \sum_{k=1}^8 \left(\sqrt{(SSUB_I^{V_{ts}}_{i,j} * k(x)^2 + (SSUB_I^{V_{ts}}_{i,j} * k(y)^2)} \right) \right\} \right] \quad (2)$$

348 where $SSUB_I^V EGM_{i,j}$ is the set of *max* and *mean* EGM values for image I , sub-variable set V
 349 (e.g., $SSUB_I NDVI$), at pixel location i, j . The image gradient, $(SSUB_I^{V_{ts}} * k(x|y)^2)$, for kernel
 350 pair k is computed by convolving a $SSUB_I$ time series statistic (ts) with a kernel as:

$$SSUB_I^{V_{ts}}_{i,j} * k(x|y) = \sum_{n=1}^9 (SSUB_I^{V_{ts}}_{i,j} \cdot k_{m(n)[1],m(n)[2]}) \quad (3)$$

$$m \in \{(-1, -1), (-1, 1), (0, -1), (0, 0), (0, 1), (1, -1), (1, 0), (1, 1)\}$$

351

352 where m is the set of kernel pixel offset locations relative to the image pixel location (i, j) . The
 353 EGM was computed over the set of 8 convolution kernel pairs, applied independently to each
 354 $SSUB_I$ time series statistic, and the mean and maximum EGM of the 8 EGMs were calculated to
 355 produce $SSUB_I^V EGM_{i,j}$. A crop field edge should have a high EGM maximum and mean over all
 356 sub-variables. Thus, in order to give preferential treatment to consistently high and strong
 357 EGMs, we weighted them by the *mean* and *max* EGM, followed by a gamma transform
 358 ($\gamma = 0.1$) to increase low EGM values relative to higher values (Eq. 3).

359

$$SSUB_I^V EGMW_{i,j} = \left\{ \sum_{ts \in 1,2,3,4} (SSUB_I^{V_{ts}} EGM_{i,j}^{max} \cdot SSUB_I^{V_{ts}} EGM_{i,j}^{mean}) \right\}^{\gamma} \quad (4)$$

360

In the next step, we used CLAHE to adjust and standardize the local contrast of EGM values. The CLAHE procedure is a histogram equalization applied tile by tile, as opposed to traditional histogram equalization that uses the entire image for contrast adjustment. The CLAHE approach only considers the range of data within a particular tile, and therefore produces a transformation function for each tile, relevant at the tile's center pixel. All other pixels within the tile are bi-linearly interpolated with the adjusted tile center values, for computational efficiency and to produce smooth transitions between tile borders. The 'contrast limited' portion of the method is derived from clipping the local histograms to predetermined thresholds prior to computing the cumulative distribution function (Zuiderveld, 1994). We used a range of tile sizes (5 x 5, 7 x 7, 9 x 9, or 150m x 150m, or 210m x 210m, and 270m x 270m, respectively) and clip percentage limits (1, 2.5, 5), and then used the mean adjustment over all combinations (i.e., 9 iterations):

$$SSUB_I^V CLAHE_{i,j} = \frac{\sum_{\substack{t \in \{5,7,9\} \\ cp \in \{1,2.5,5\}}} \left\{ CLAHE(SSUB_I^V EGMW_{i,j})_{t,cp} \right\}}{9} \quad (5)$$

where $SSUB_I^V CLAHE_{i,j}$ is the locally CLAHE adjusted EGM at pixel location i, j , at CLAHE tile size (t) and clip percentage threshold (cp) pairs. Next, we applied a binary, edge or no-edge, threshold to the CLAHE results using an adaptive threshold (ATh) approach. As mentioned, a single threshold value cannot be consistently applied to an entire image or image region. Therefore, we used ATh to convert object edges to binary edge or no-edge values. For each local tile, a threshold value was considered from the local pixels only. A threshold was explicitly

computed (as opposed to interpolated) for each pixel, for each local tile centered around pixel i, j . We used the tile median EGM to determine the threshold at scale t . The binary object edge estimate for image I is thus:

$$SSUB_I AT_{i,j} = \begin{cases} 1, & \text{if } EGM_{i,j}^b > 0 \\ 0, & \text{otherwise} \end{cases} = EGM_{i,j}^b = AdaptThresh(M_{i,j})_t$$

where, $M_{i,j} = \sum_{V \in SSUB_I} \{M_{i,j} = SSUB_I^V CLAHE_{i,j} \cdot M_{i,j}\}$, where, $M_{i,j} =$ (6)
1 if $V = 1^{st}$ $SSUB_I$ variable

where $SSUB_I AT_{i,j}$ is either a land cover edge or no-edge and $AdaptThresh$ is the ATh procedure at scale $t = 25$. The EGM results are cumulatively combined (M) by taking the product of each successive CLAHE process, where M is initialized at 1.

3.3.2 Edge morphological cleaning

After adaptively thresholding image edges, we applied a series of morphological thinning (Lam et al., 1992), endpoint linking, and endpoint trimming to clean edges. First, we morphologically thinned the cumulative edges with 1 iteration. Then gaps between endpoints were closed by linking the shortest path between the two endpoints following a set of rules: 1) gaps between two endpoints that were less than 4 pixels wide were closed; 2) gaps between two endpoints that were between 4 pixels and 8 pixels wide were closed if the endpoints were at inverse angles. Here, we estimated the directional angle of each endpoint and considered inverse rounded angle pairs as 0 and 180, 45 and 225, 135 and 315, and 90 and 270 degrees; 3) gaps between an endpoint and an edge that were greater than 8 pixels wide were closed if there was

400 sufficient EGM (mean EGM > 0.1) along the shortest connecting path and the endpoints were at
 401 inverse angles, as described in the second criteria. This last check was to ensure field
 402 boundaries with true gaps were not incorrectly closed. The connecting path between endpoints
 403 was determined by the shortest distance between endpoints that did not cross land cover
 404 edges. After thinning and closing small gaps, the final edges were thinned with a morphological
 405 skeleton operator, which is morphological thinning with infinite iterations (Zhang and Suen,
 406 1984), that ensured all edges were a maximum of 1 pixel wide. The final edge image after the
 407 morphological cleaning process is:

$$SSUB_I Objects_{i,j} = \overset{1 \text{ if}}{inverse(EGM_{i,j}^b) > 0.45ha} = EGM_{i,j}^b = Clean(SSUB_I AT_{i,j}) \quad (7)$$

408
 409 where $SSUB_I Objects_{i,j}$ is the final binary object estimate for image I , at pixel i,j , and $Clean$ is
 410 the morphological cleaning operations of thinning, endpoint linking, and skeleton. The final
 411 procedure ($inverse$) was an inversion of edges to objects and the removal of small objects with
 412 a predetermined threshold of 5 pixels (~0.45ha) for the minimum field size. The lower threshold
 413 was determined from visual observation of the minimum detectable object from Landsat in the
 414 study region. The steps described above are illustrated in rows A—D of Figure 6.

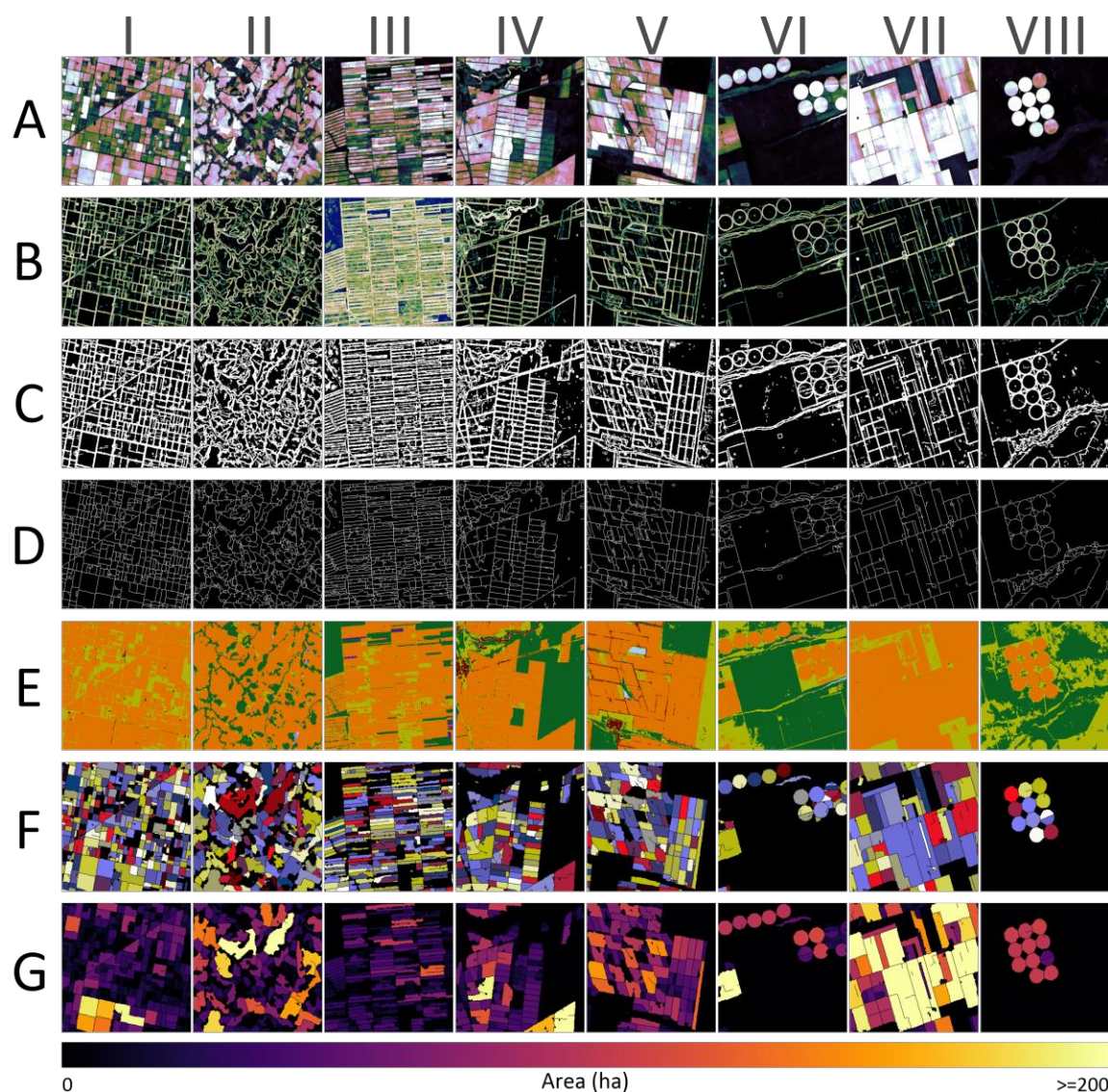


Figure 6. Principal steps of the field extraction process. Each row represents a step in the workflow and each column a sample grid within the test region. The methodological steps are: A) Time-series variable, NDVI CV, smoothed with a bilateral filter; B) Edge gradient magnitude after multi-scale CLAHE normalization; C) Binary edges after multi-scale adaptive thresholding; D) Binary edges after morphological cleaning; E) Thematic land cover classification (orange illustrates cropland); F) Land cover objects after intersection with cropland (color display is random); and G) Field parcels after intersection with cropland, where the field size is illustrated according to the color ramp on the bottom. The center coordinates for each sample grid are: I) $-31^{\circ} -59' -9.44''$ S, $-61^{\circ} -57' -58.57''$ W; II) $-27^{\circ} -45' -12.89''$ S, $-53^{\circ} -21' -8.83''$ W; III) $-17^{\circ} -12' -45.13''$ S, $-62^{\circ} -8' -24.1''$ W; IV) $-24^{\circ} -44' -25.49''$ S, $-64^{\circ} -8'$

424 -42.96" W; V) -25° -26' -2.47" S, -63° -44' -56.13" W; VI) -12° -52' -12.8" S, -45° -40' -39.62" W; VII) -12° -38' -57.96"
425 S, -46° -10' -40.07" W; VIII) -12° -50' -42.67" S, -45° -23' -36.3" W.

426

427 3.4 Field labeling

428 The object extraction approach using localized edge thresholding was fully automated, whereas
429 we used a semi-supervised approach to label objects as cropland or not. We collected samples
430 for 9 land cover categories (Cr=cropland; Pg=pasture/grassland; Tr=trees (natural); Ub=Urban;
431 Wt=Water/Wetland; Ba=Bare; Sh=Shrub; Pl=trees (plantation); and Cl=Cleared trees (during
432 study timeframe)), and used the samples collected across the study region to train a supervised
433 predictive model to estimate cropland and non-cropland land covers from S_I . Land cover was
434 sampled similarly to Graesser et al. (2015), yet whereas the reference study was restricted to
435 high-resolution imagery, this study supplemented high-resolution acquisition gaps by sampling
436 directly from Landsat imagery. As in Graesser et al. (2015), Latin America regional experts and
437 image interpretation experts used high-resolution imagery from Google Earth and the Landsat
438 time series composites to distinguish between the 9 land covers.

439 We used the classification model, Extremely Randomized Trees (ERT) (Geurts et al.,
440 2006), which is an ensemble of randomized decision trees similar to Random Forests (RF)
441 (Breiman, 2001). However, rather than bootstrap sampling as typically performed in RFs, the
442 entire set of samples is used in each tree with ERT. Additionally, a RF searches for the best split
443 from a random subset of predictor variables, whereas an ERT randomly chooses a split, typically
444 resulting in smoother decision boundaries in feature space. We used the Scikit-learn
445 implementation of ERTs (Pedregosa et al., 2011) to construct the predictive land cover model.

To identify individual crop fields, per-pixel cropland estimates were intersected with the segmented objects described in section 3.3.1. If estimated cropland pixels accounted for 50% or more of a segmented object, the object was identified as a crop field. Otherwise, the object was removed.

We conducted a predictor variable ranking and ERT parameter optimization prior to training the classification model. First, we ranked the importance of all fifty possible predictor variables from S_I with a χ^2 test (Liu & Setiono, 1995) and the ERT feature importance, and removed features that fell in the lower 50th percentile of both of the respective ranking methods, resulting in fourteen of the fifty possible predictor variables removed. This reduced predictor set was supplemented with Shuttle Radar Topography Mission (SRTM) 1 arc-second (~30 m) elevation and slope data, as well as x, y coordinate information of each sample, culminating in forty predictors. Then, we applied a 5-folds cross-validation of a range of ERT parameters on the forty predictor variables. At each fold, 50% of the land cover samples were randomly selected with replacement. We then tested the overall accuracy on the samples withheld after each parameter combination of trees (500 and 1,000), maximum depth (5, 10, 15, 20, 25, 30, and 50), and minimum samples to split a node (2, 5, and 10). The parameter combination with the highest overall accuracy on withheld samples was 500, 30, and 2 for trees, maximum depth, and minimum samples, respectively, and we used defaults for the remaining parameters. This final set of parameters was used to train an ERT model using all available land cover samples.

3.5 Validation & assessment

3.5.1 Sampling & assessment

We conducted two accuracy assessments: 1) an assessment of the thematic map accuracy of the cropland ERT estimates; and 2) an object-based assessment of randomly stratified fields throughout the study region to evaluate the field parcel accuracy. For the thematic land cover assessment, we assessed model performance on 30% of the samples randomly withheld from the ERT model. Note that the model assessment on 30% of the withheld samples was conducted post-parameter optimization (section 3.4) on the final parameter set, and not on cross-validated samples.

We also assessed the local error of the land cover map by using the complete set of land cover samples with a spatially constrained systematic sampling approach following methods described in Foody (2005), and illustrated in Figure 7. For the spatially constrained map assessment, we systematically created a point grid of local assessment locations every 200 km across the study area. At an assessment location, we recorded the n -nearest ($n=100$ for this study) land cover samples described in section 3.4. We constrained the sample search by limiting the maximum search distance to 300 km around each assessment location. The cropland class f -score, a weighted average of the producer's and user's accuracy ($f\text{score} = 2 * \frac{\text{Producers} * \text{Users}}{\text{Producers} + \text{Users}}$), was then recorded for those n -nearest 100 land cover samples, at an assessment location. This was repeated for all assessment locations, and the cropland f -scores were interpolated to create a continuous grid for the entire study area. We used the f -score in place of overall (or global) accuracy because the cropland class was of most interest for this

study. The subsequent grid is indicative of model fit rather than map accuracy because we used the same set of samples to train the classification model.

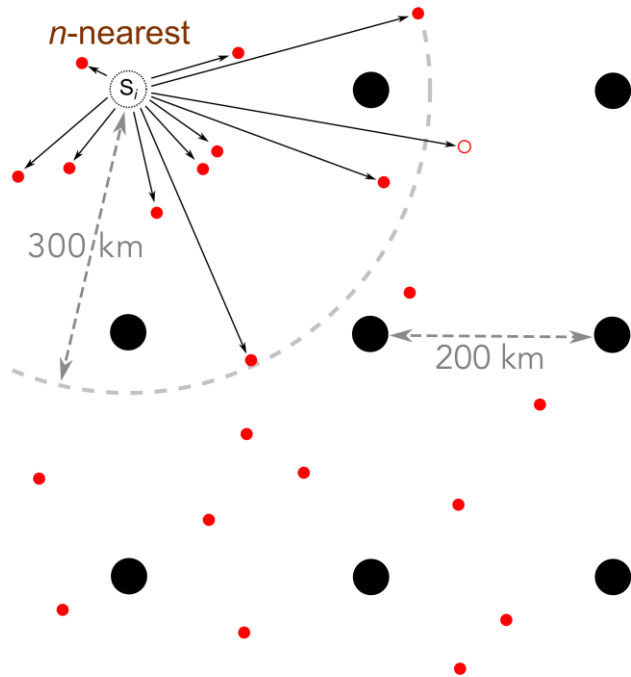


Figure 7. Spatially constrained systematic sampling for thematic accuracy assessment. At each sample location (black dots, currently at s_i), the n -nearest land cover samples (red dots) are selected for map assessment. The local assessment scores are stored at each sample location. The land cover sample selection is first limited to the n -nearest samples and then by the search radius around the current sample location (here, set at 300 km).

For the object-based assessment we created wall-to-wall 10 km x 10 km grids across the test region and randomly selected 1,000 grids with at least 10% crop area (estimates based on 2000/2001 Landsat cropland estimates from this study) (Fig. 1). Our goal was to have more crop field samples throughout the entire region rather than many samples from one area. Using the Landsat time series composites and Google Earth imagery, we manually digitized at least 2 fields within each grid for a total of 5,480 validation field parcels, limiting delineated parcels to

those in which we had high confidence that they were indeed crop fields. In each grid, we included the range of field sizes and shapes found throughout the study region. Moreover, we attempted to delineate fields with ‘weak’ edges or where field interiors were not clean. Still, an entire field must be visible for an interpreter to identify it from imagery. Thus, we did not include all fields within each grid.

Traditional per-pixel validation approaches are not appropriate for object-based validation. Instead, we assessed individual field parcels following proposed metrics (Persello and Bruzzone, 2010; Whiteside et al., 2014; Yan and Roy, 2014). Land-cover objects can be evaluated based on location (the spatial coherence between a predicted and reference object) and overlap (over- and under-segmentation, shape comparison). The Euclidean distance of object centroids was used to measure offset errors, while over- and under-segmentation, fragmentation, and shape eccentricity were used to measure object overlap and shape errors. We only considered overlapping objects when evaluating these object-based metrics. That is, for each reference object we extracted all overlapping, predicted objects. Only the object with maximum overlap was used for over- and under-segmentation, whereas all overlapping predicted objects were considered with fragmentation (see Persello and Bruzzone (2010) for detailed explanation). In Persello and Bruzzone (2010), error metrics are defined in a 0-1 dynamic range, with perfect agreement being values of 0. We express error metrics in inverted percentages (i.e., $(1 - error) \times 100$). Therefore, perfect agreement equals 100.

3.5.2 *Field distribution curves*

To evaluate inequality in field size distributions, we plotted Lorenz curves (Lorenz, 1905) (commonly used to show economic inequality) of field parcel sizes within each province. The Lorenz curve shows the crop field deciles in a province on the x-axis versus the cumulative percentage of total cropland on the y-axis. We computed the Gini index (as a measure of field size inequality) from the Lorenz curve as: $Gini = (\frac{A}{A+B})$, where A is the area between the 1:1 line and the plotted distribution (Lorenz curve), and B is the remaining area under the curve. The Gini coefficient ranges from 0 to 1, where 0 is equally distributed and 1 is high inequality.

4. Results

4.1 *Composite, cropland, & field parcel estimates*

The seasonal compositing resulted in seamless path/row boundaries throughout the study area, which allowed the use of a single classification model and limited artificial image edges. Two subsets of the composites illustrate the effectiveness of the normalized CDR surface reflectance products to produce a standardized continental Landsat dataset (Fig. 8). The CV and the 50th and 75th percentiles illustrate the seasonality fluctuations of row-crop agriculture. Generally, dark blue and purple shades are those with high seasonal variance and low to medium 50th and 75th percentile values, and pink illustrates land cover with a high CV and high 75th percentile. Stable values are generally shades of yellow, where the CV is very low and the 50th and 75th percentiles are high.

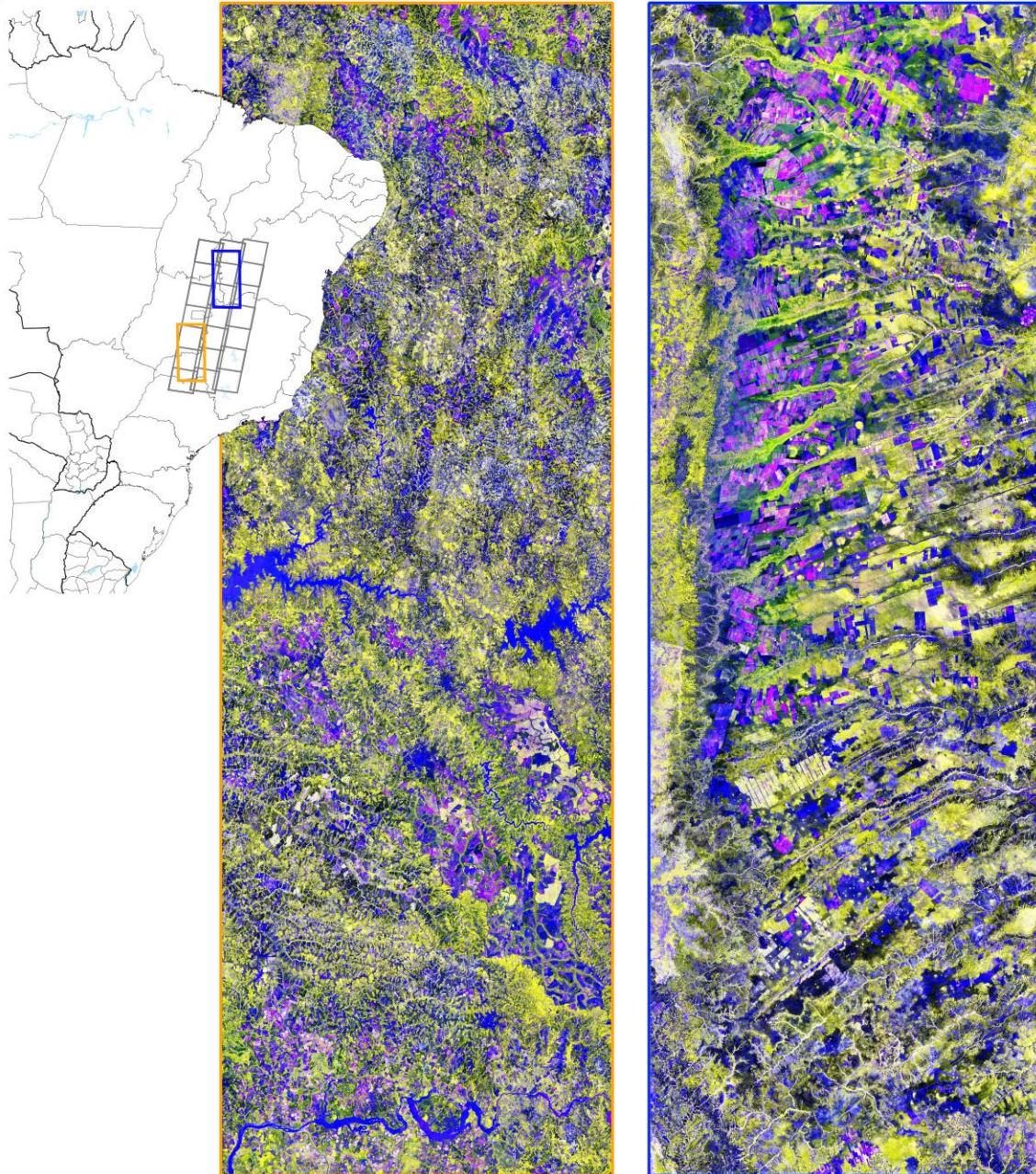


Figure 8. Examples of annual composites, with the 75th percentile displayed as red, the 50th percentile displayed as green, and the coefficient of variation displayed as blue. Each location shown, highlighted by a blue or orange frame in the top left inset, covers an area of 450 km x 150 km. The gray overlapping grids illustrate overlapping Landsat path/row grids.

548 The thematic cropland results capture the key cropland areas of the study area and the
549 detection of individual field parcels illustrates the broad range of field sizes across this vast area
550 (Fig. 9). Small fields and larger (displayed in shades of green and orange) are distributed
551 throughout the study area, but generally more prevalent in the southern half. In southern
552 Argentina and southern Brazil, small fields tend to be mixed with larger fields (shades of blues),
553 but the broad pattern is one of large-to-small fields emanating from core areas. For example,
554 the densest cluster of small fields in the Argentine Pampas is in central Santa Fe province, on
555 the northern fringe of the agricultural core. Elsewhere in Brazil's most southern state, Rio
556 Grande do Sul, small fields surround larger fields in the main agricultural centers. This pattern is
557 also similar through the Brazilian states of Santa Catarina, Paraná, and São Paulo, and to some
558 extent in Santa Cruz, Bolivia. However, newer agricultural regions have contrasting field
559 arrangements. For example, the configuration of larger fields is more prominent in the
560 Argentine Chaco (Salta and Santiago del Estero provinces), with the exception of small fields in
561 the Andes foothills. Similarly, the u-shaped agricultural belt in the Brazilian Cerrado, covering
562 states of Mato Grosso, Mato Grosso do Sul, Goiás, and Bahia, consists principally of fields
563 around, or larger, than 100 ha. Finally, results for central Chile and southwestern Uruguay
564 illustrate landscapes dominated by small fields during the 2000/2001 timeframe.

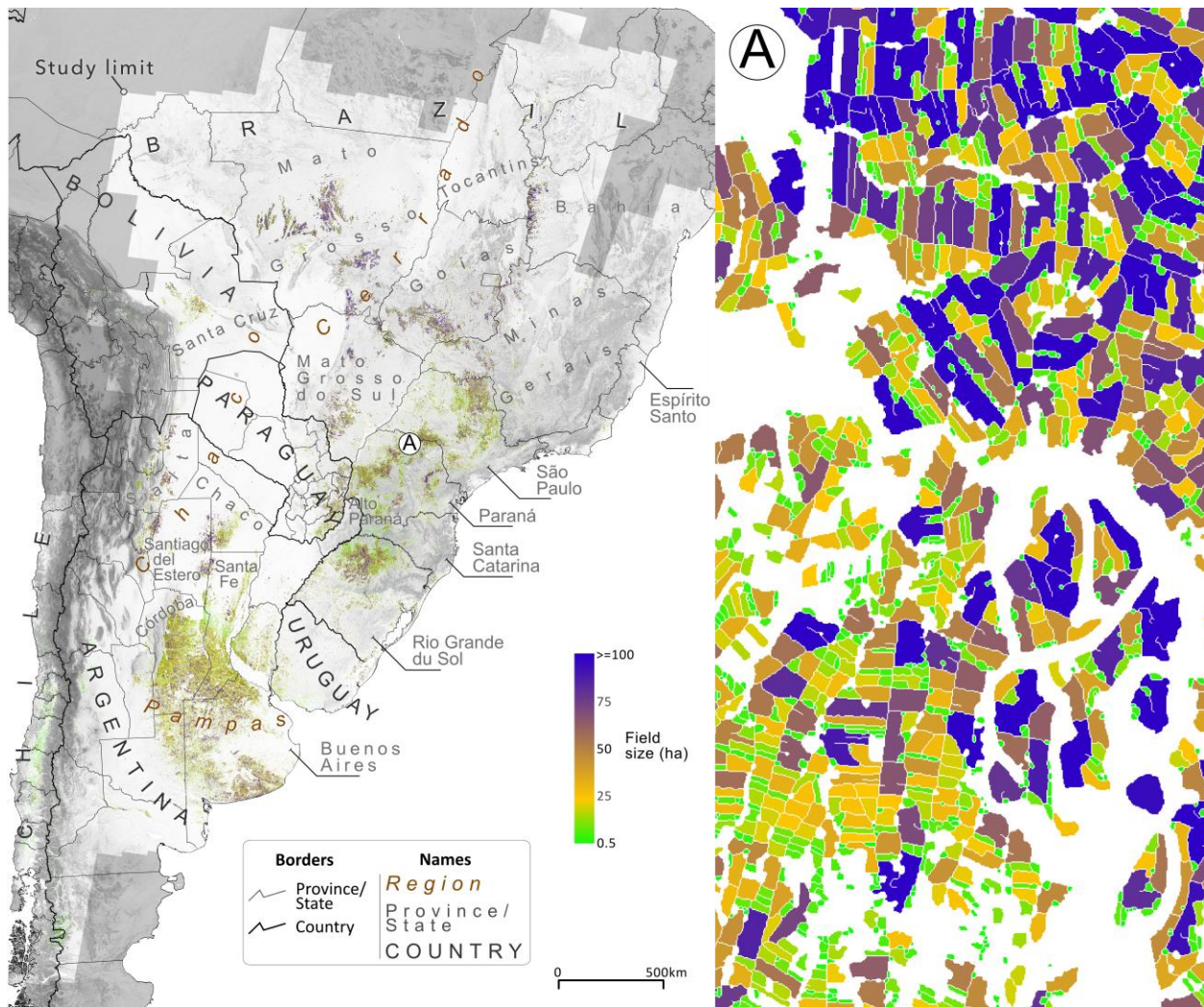


Figure 9. Cropland and field size results for the January 1, 2000 to August 1, 2001 period. Here, the cropland footprint is shown by field size and is illustrated by non-gray colors. The right inset shows a large-scale map view of marker A in the left map.

Figures 10 and 11 illustrate crop field extraction results at a larger scale than shown in Figure 9. The 3-band time series sub-samples showcase the importance of seasonal information for cropland detection. In the center column, detected fields are displayed by random colors, while in the right column, detected fields are displayed by area, on a scale of 0.45 to ≥ 100 ha (0, or black, is non-cropland). Many small fields (although small may be relative for this part of

574 the world) exist in the core agricultural region of Argentina. Small and large fields are mixed
575 throughout the Argentine landscape, as illustrated in the Río de la Plata basin, where there are
576 many fields less than 10 ha (Fig. 10). Elsewhere, in the main agricultural region of Rio Grande du
577 Sol, Brazil, the field size range spans the entire scale spectrum, but very large fields dominate
578 this landscape (Fig. 11). A noticeable difference between the Brazilian example (Fig. 11) and the
579 Argentine example (Fig. 10) is the field morphology, or shape. The flat, Argentine Pampas
580 allows for regularly gridded farming patterns, whereas a much different pattern exists in
581 southern Brazil, where field shapes follow tree corridors, water bodies, and the topography.
582 Elsewhere throughout the region, settlement patterns produce a complex agricultural
583 landscape, with very small fields approaching the limitations of Landsat's detectable scale. In
584 some agricultural landscapes, such as in Santa Cruz, Bolivia, fields approaching 5 ha and smaller
585 are more difficult to detect because they are long and narrow.

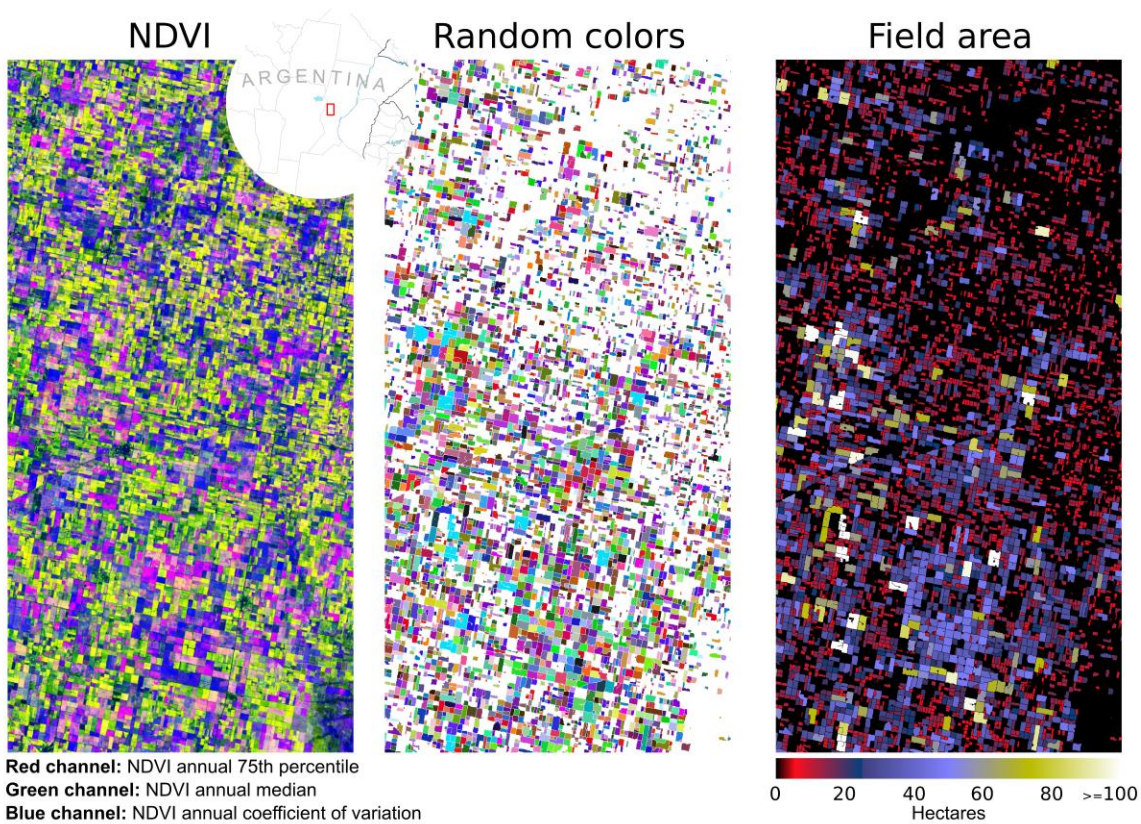


Figure 10. Field extraction examples from Santa Fe province, Argentina. **Left column:** RGB display of temporal statistics computed from 1.5 years of Landsat imagery. Generally, blue, purple, and pink represent row-crop agriculture, green and blue represent pastures, and yellow represents trees. **Center column:** Field extraction results, displayed by random colors. **Right column:** field extraction results, colored by increasing field size. Each inset is 60 km x 30 km.

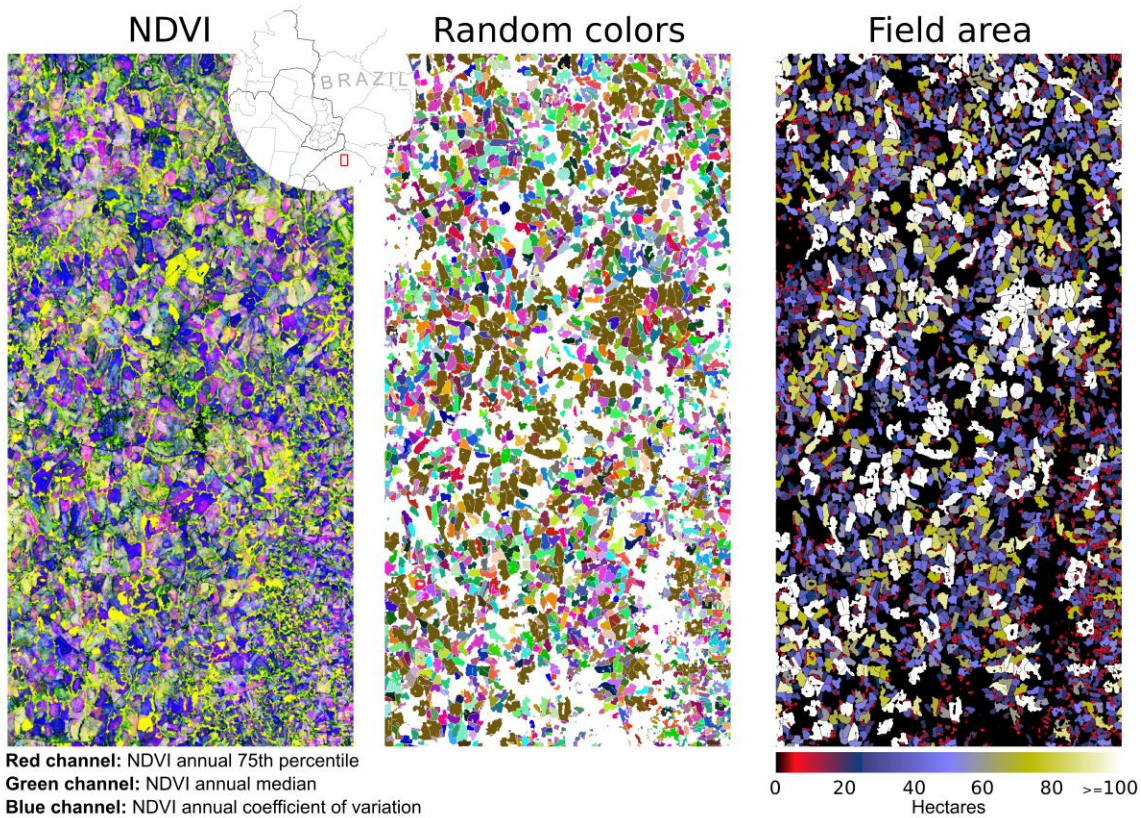
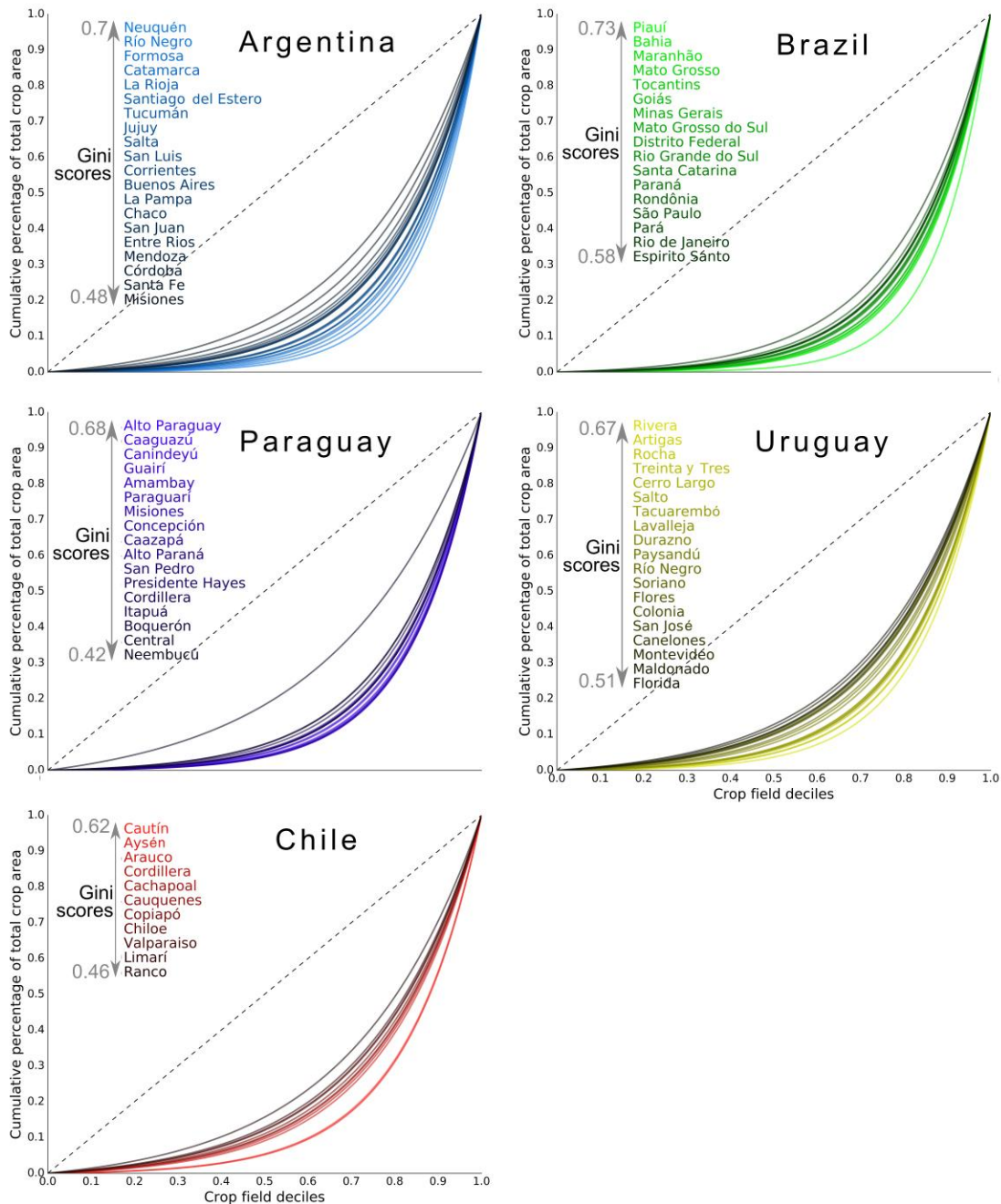


Figure 11. Field extraction examples from Rio Grande do Sul state, Brazil. **Left column:** RGB display of temporal statistics computed from 1.5 years of Landsat imagery. Generally, blue, purple, and pink represent row-crop agriculture, green and blue represent pastures, and yellow represents trees. **Center column:** Field extraction results, displayed by random colors. **Right column:** field extraction results, colored by increasing field size. Each inset is 60 km x 30 km.

Field size distributions at the second administrative unit (i.e., provincial or state) are shown for 5 countries (Figure 12). The figure illustrates the provincial-level Lorenz curves and Gini coefficients of field size for each country. The highest Gini scores (i.e., most unequal distribution of cropland by field size) among all administrative units assessed were in Piauí, Brazil (0.73), Neuquén, Argentina (0.70), Alto Paraguay, Paraguay (0.68). The high Gini scores are illustrated by the dominance of large fields in the respected provinces (Fig. 9). Provinces

605 with cropland dominated by large fields are found in Argentina, Brazil, and Paraguay. However,
606 Chile and Uruguay show more equal distributions of small fields, which noticeably dominate the
607 cropland landscape (Fig. 9).



608

609 Figure 12. 2000/2001 field size distributions in selected second level administrative units (province or state) in
 610 Argentina, Brazil, Chile, Paraguay, and Uruguay. Lorenz curves and Gini coefficients of provincial-level field size
 611 distributions. The x-axis represents the cumulative crop field deciles within a province, while the y-axis represents
 612 the cumulative percentage of total crop area at each decile. The colors illustrate the province's Gini coefficient

scores (1=unequal distribution of cropland area toward large fields; 0=equal cropland distribution among all field sizes).

4.2 Map and object accuracy

The thematic cropland accuracy assessment resulted in cropland producer's, user's, and f-scores of 90.7%, 97.1%, and 91%, respectively (Table 2). The other classes included in the classification model are also shown but not highlighted, along with overall (84%), kappa (0.8), and the sample-adjusted (Olofsson et al., 2013) overall score (88%). Figure 13, panel A shows the results of the f-score spatially constrained assessment. Cropland f-scores were in the upper 90s across the region, indicating a spatially well-balanced and generalizable predictive model. Pockets of poorer estimates, such as in central Chile, decreased the overall f-scores (Table 2).

In general, over-segmentation errors were worse than under-segmentation (Table 3), particularly on the northwestern and northeastern fringes of the study region (Fig. 13, panels B-C). The highest under-segmentation errors were in and north of São Paulo, Brazil. Overall, object-based errors are clustered near the ideal target of 70 and higher (Fig. 14). Segmentation and fragmentation errors decrease as field size enlarges (top left and bottom left insets). However, the eccentricity shape error and centroid offset do not indicate any relationship with field size (top right and bottom right insets).

634 Table 2. Error matrix for thematic classification results (From section 3.4: Cr=cropland; Pg=pasture/grassland;
635 Tr=trees (natural); Ub=Urban; Wt=Water; Wd=Wetland; Ba=Bare; Sh=Shrub; Pl=trees (plantation); Cl=Cleared trees
636 (during study timeframe)). Nine land cover classes were sampled, but we highlight cropland (in gray) for the
637 purposes of this study's interests. (UserA and ProdA refer to sample-adjusted producer's and user's accuracy,
638 respectively, following Olofsson et al., (2013); *=Overall accuracy; **=Kappa score; ***=Sample-adjusted overall
639 accuracy).

		Observed												
		Cr	Pg	Tr	Ub	Wt	Ba	Sh	Pl	Cl	Total	User	UserA	
Predicted	Cr	997	9	1	4	3	--	--	13	--	1,027	97.1	97.1	
	Pg	91	1,002	24	55	8	6	32	8	3	1,229	81.5	81.5	
	Tr	10	8	946	8	1	--	--	30	2	1,005	94.1	94.1	
	Ub	--	2	--	620	--	8	--	1	--	631	98.3	98.3	
	Wt	--	--	--	--	244	2	--	--	--	246	99.2	99.2	
	Ba	--	2	--	1	39	86	2	--	--	130	66.2	66.2	
	Sh	--	2	1	1	--	3	152	--	--	159	95.6	95.6	
	Pl	--	--	3	--	--	--	--	93	--	96	96.9	96.9	
	Cl	1	--	1	--	--	--	--	--	50	52	96.2	96.2	
	Total	1,099	1,025	976	689	295	105	186	145	55				
Prod		90.7	97.8	96.9	90	82.7	81.9	81.7	64.1	90.9	*84 **0.8			
ProdA		67.5	98.8	97.2	32.2	56.2	78.7	78.9	8.1	25	***88.1			

640

641

642

643 Table 3. Object assessment summary of 5,480 fields. The range of over- and under-segmentation, eccentricity
644 error, and fragmentation is 0 to 100, with 100 being perfect agreement. The offset error is given in meters.

	Over- segmentation	Under- segmentation	Eccentricity	Fragmentation	Offset	Relative % error
μ	68.02	86.58	90.23	99.85	7.18	-10.07
50 th percentile	75.96	94.44	95.26	99.89	2.98	-16.78
Number of Fields greater than μ	3,473	4,346	3,730	3,340	4,098	3,574
Percentage of fields greater than μ	63	79	68	61	75	65
Margin of error ($p=0.05$)	± 0.64	± 0.63	± 0.34	± 0.004	± 0.29	± 2.03

645

646

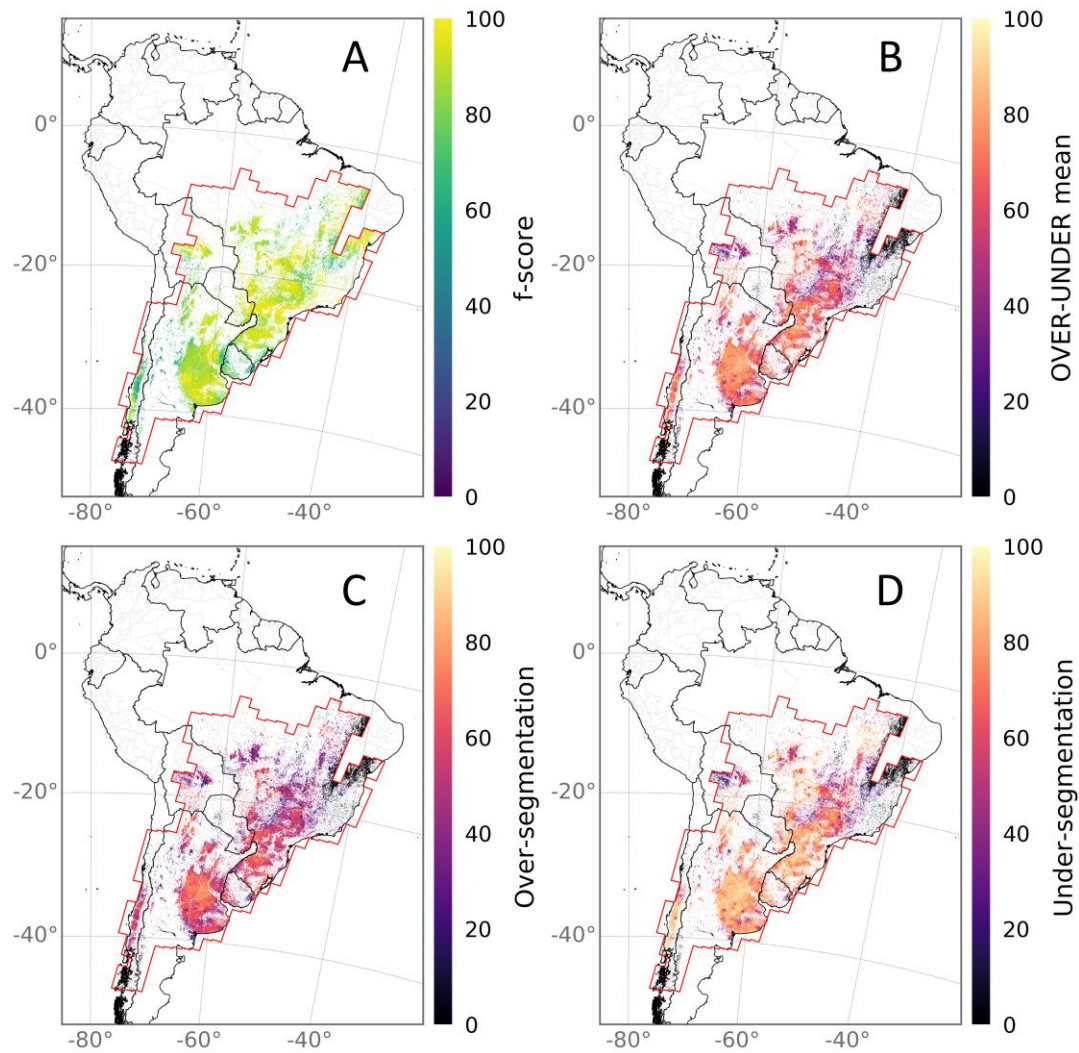


Figure 13. Spatially constrained errors of: **A)** Cropland f-scores (the f-scores are scaled to percentages). For every systematically sampled point location (200 km spacing), the local cropland f-scores of the n -nearest ($n=100$) land cover samples was calculated. The results for all points were then interpolated to produce a continuous error estimate for the entire study area. The points used for accuracy assessment were the same points used to train the classification model, thus the illustration is a better representation of model accuracy than map accuracy; **B)** Mean of over- and under-segmentation. **C)** Over-segmentation; and **D)** Under-segmentation. Each metric was masked by a 1,000 m x 1,000 m grid of cropland, where areas in white do not contain any cropland.

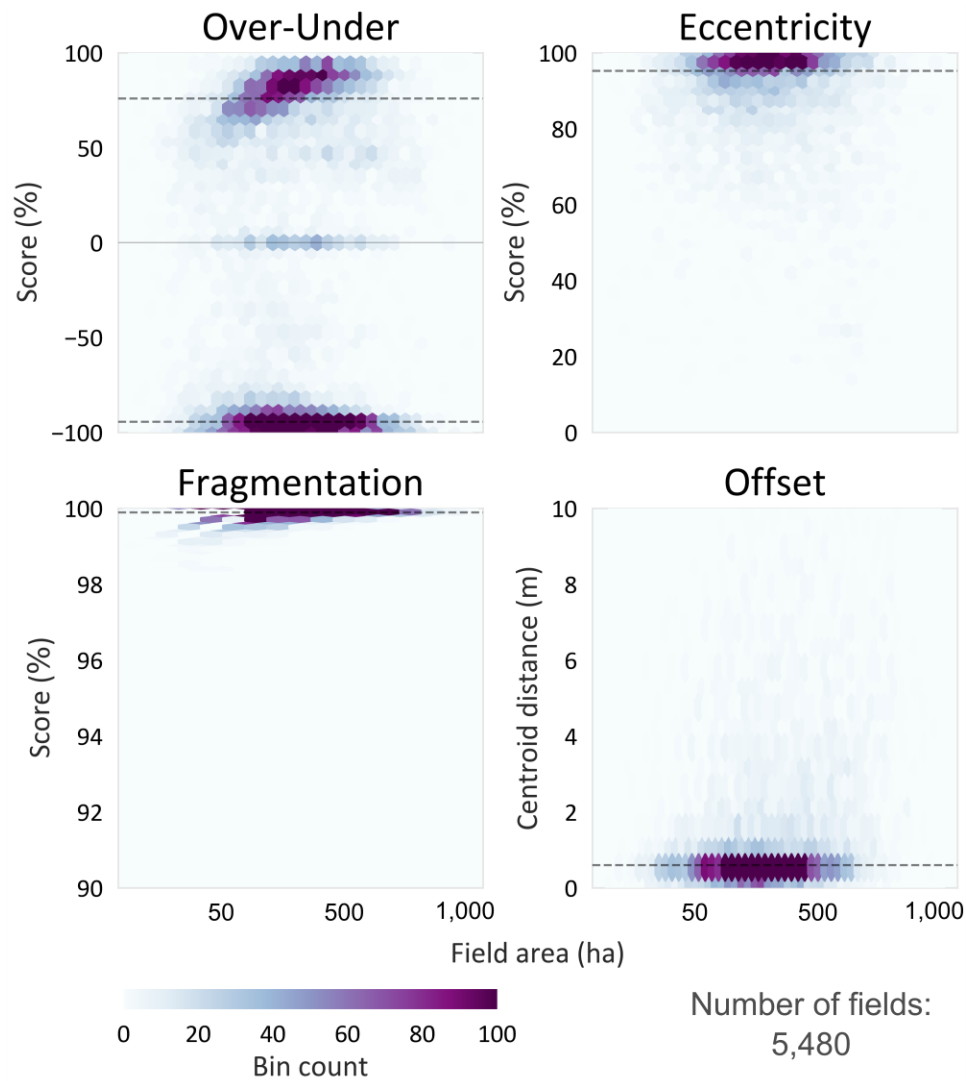


Figure 14. Object accuracy binned scatterplots. For each object metric, 5,480 manually delineated fields were assessed against the predictions of the crop extraction algorithm. The best possible score for the ‘Over-Under’, ‘Eccentricity’, and ‘Fragmentation’ metrics is 100, whereas the distance metric is optimal at 0. The dashed lines represent the median score for the respective metrics. **Top left:** Over- and under-segmentation. Note that over-segmentation ranges from 0 to 100, while under-segmentation was inverted (0 to -100) for illustration purposes. **Top right:** Eccentricity shape error (range 0 to 100). **Bottom left:** Fragmentation error (range 0 to 100). **Bottom right:** Distance offset (units in meters). The x-axis is logged for display, with real units shown.

5. Discussion

Cropland mapping is often reliant on a seasonal profile to accurately distinguish it from other vegetation. Previously, dense time series stacks were a major limitation with the Landsat satellite because of computational limitations and the cost and access to Landsat imagery (Woodcock et al., 2008). The opening of the archive and computational advancements have since made Landsat a more viable option for regional (Yan and Roy, 2016) and global earth observation (Hansen et al., 2013). As shown from Figure 9 and Table 2, the extent of cropland can be accurately estimated in South America using multi-temporal Landsat imagery, and is comparable to MODIS cropland estimates that utilized higher temporal but coarser spatial resolution (Graesser et al., 2015). At the field parcel level, the object validation showed that parcels can be extracted across a large region. Additionally, the more general field-size patterns across the region illustrated that the older, traditional agricultural regions of southern Brazil, Santa Cruz, Bolivia, and the Argentine Pampas comprise a wide range of field sizes, whereas the newer agricultural frontiers of northern Argentina and the Brazilian Cerrado have a greater presence of large fields. This is also reflected in the Lorenz plots, where there is a larger distribution spread in administrative units closer to the agricultural frontiers.

5.1.1 Temporal challenges

In this study, we extracted field parcels for the period January 1, 2000 to August 1, 2001. This timespan presented few limitations to data coverage and sensor issues (Kovalskyy and Roy, 2013). However, time series compositing with pre-2000s Landsat data will prove more challenging because of less coverage over the South American continent. Moving forward,

Landsat availability for the 21st century is generally plentiful. However, while applications of post-2000 field detection can utilize the ETM+ sensor, SLC-off corrections will be imperative in order to eliminate potential artificial field boundaries introduced from the scan line errors. This will be an important challenge for detecting fields in the SLC-off/pre-Landsat 8 period. While linear interpolation might suffice for uses such as visual aid and per pixel land cover classification, it will likely hinder object segmentation methods. Gap-filling methods that utilize spatial context are more promising. We consider two such methods that have proven to provide better estimates of missing data gaps: 1) Geostatistical kriging (Zhang et al., 2007) and 2) the USGS Phase 2 method (USGS, 2004). Both of these methods use neighboring pixels from multiple scenes to fill SLC-off data gaps. Future work should assess the tradeoffs between the Zhang et al. (2007) method, which is more statistically rigorous, but more computationally intensive, and the USGS Phase 2 least squares approach. The recent launches of Landsat 8 and Sentinel-2 series should ensure continued broad temporal coverage at a sub-30 m scale beyond the SLC-off period, though.

5.1.2 Spatial challenges

At 30 m spatial resolution, Landsat can be used to detect a large range of field sizes, and much of the sub-Andean row-crop agriculture in our study area is at or above Landsat's minimum size requirements. However, fields smaller than 1 ha are not as reliably detected, depending on the field's configuration. In the Argentine Pampas, for example, the gridded settlement, road, and agricultural patterns produce many uniform-sized fields. Thus, fields around 0.5 ha are detectable. However, land cover objects are only detectable if there is sufficient separation

708 between an object's interior and its edges. Otherwise, the object simply becomes a line.
709 Elongated fields under 1 ha are more challenging to detect because of a lack of separability in
710 the object's interior. In addition to field size, shape, and configuration, another obstacle to
711 accurately identify field boundaries is crop type. In the absence of natural or man-made
712 borders such as streams, wetlands, or roads, field parcel detection is reliant on the detection of
713 salient features to distinguish one crop from another. Neighboring crops may often be different
714 species types (e.g., maize or wheat), and therefore have different growing patterns. Or, the
715 crop's temporal signature may be sufficient to identify boundaries. However, when neighboring
716 crop fields are of the same species or are only separated by a small gap or fence line, the
717 minute separation becomes saturated at the Landsat scale.

718 These scale impediments were illustrated in the object accuracy results, where the worst
719 observed scores were in the main sugarcane region of Brazil and in northeastern Brazil.
720 Sugarcane is challenging to segment because of the homogeneous connectivity from field to
721 field (especially in the absence of fence lines), as well as the terraced planting methods
722 employed by farmers. In some cases, even high-resolution imagery is not sufficient to visibly
723 distinguish between field boundaries in this region. In northeastern Brazil, the scale of
724 agricultural production affected the results, where very small-scale agriculture led to poor
725 results in the region. An obvious solution to the issue of very small fields or subtle borders is the
726 employment of higher-resolution imagery. If the tradeoffs between spatial, temporal, and
727 radiometric resolution do not limit the parcel detection, then Landsat's panchromatic band
728 (15m) and the newly launched Sentinel-2 (10m and 20m) could be valuable for future field
729 extraction. Future work on field parcel detection from satellite imagery should utilize the

growing resource-base of high-resolution imagery, as well as assess possibilities for algorithmic improvement to reduce over-segmentation errors.

5.1.3 Large-scale estimates beyond land cover

Rich satellite datasets and technological advancements are changing the nature in which we can observe and monitor vegetation across the planet (Hansen et al., 2013). However, global datasets, especially agricultural land cover maps, still lack in precision and detail (Fritz, 2013). Information that describes agriculture beyond area, such as agricultural intensification, is especially absent (Kuemmerle et al., 2013). Land cover maps that describe agricultural area are not sufficient to improve our understanding of rapidly changing agricultural landscapes (Vallejos et al., 2015). Global agricultural expansion has slowed in recent decades, and future agricultural changes will likely stem from greater intensification rather than expansion. Remote sensing, image processing, data storage, and compute infrastructures can provide the capacity to improve agricultural datasets at the field level (Fritz et al., 2015; Yan and Roy, 2015). The scientific community will likely still rely on censuses and surveys for information such as agricultural inputs and mechanization, but remote sensing can contribute a great deal toward monitoring of agricultural intensification, crop rotations, and crop productivity, often in near real-time.

5.1.4 Caveats and uncertainties

The cropland field object accuracy assessment was objective in the sampling of the 10 km x 10 km grids (Figure 1), but not in the field delineation within the 1,000 randomly sampled grids. Our decision to include parcels that we had high confidence in was a subjective one. Given a lack of ground data about crop boundaries for South America, we considered this the best option to assess the method over a large region. Moreover, any field manually delineated from satellite imagery is biased from human image or photo interpretation. Though it is more costly and time consuming, future work should make use of ground-collected field data for optimal and unbiased validation.

6. Summary & conclusion

The methods presented in this paper describe the detection of individual crop field parcels from multi-temporal Landsat imagery across a large region of South America. We employed a multi-directional and multi-spectral object extraction technique that was able to identify cropland field parcels at a high percentage, intersected with thematic cropland estimated at a rate of 91% (f-score). We performed two levels of assessment to address whether the methods could prove robust across varying landscapes and field types. The two, per-pixel thematic and object-based, validation assessments were spatially rigorous and included multiple ecoregions and countries. With a continuous spectrum of field-size data, we generated Lorenz curves for selected states and provinces in the study region, illustrating how the scale of farming at the field level varies among and within countries across much of South America.

We applied the experimental field detection in a continent that has experienced profound agricultural changes. South American agriculture has been at the forefront of environmental concerns, but largely because of its role in tropical deforestation. Agricultural changes have not been limited to expansion into tropical forests, or forests alone for that matter. With increasing awareness of agriculture's role in South American deforestation, plus fewer land expansion options in many areas, the remaining avenues for farmers to increase productivity are often to acquire existing cropland from other landholders, increase inputs, or sell and move to areas of expansion. There is evidence of expansion (Graesser et al., 2015), but further research is needed to identify cropland intensification from remote sensing. The methods in this study can contribute greatly to understanding the dynamics of agricultural changes, whether they be extensive in the form of forest or grassland clearance, or intensive in the form of increased mechanization, scale of production, or altered crop rotations.

Agricultural technological advancements are changing the face of farming across the globe. Global deforestation watchdogs, data access, and computational improvements have augmented our understanding of expansion into grasslands and forests. Perhaps as important, though, are the results of land *use* changes and the implications for a host of environmental issues. Agro-industrialization is changing how food is grown across the globe, yet it is not easily observed with current monitoring programs. Satellite data availability, advanced image processing techniques, and computational advancements will continue to be valuable resources to help fill this data gap.

791 **Acknowledgements**

792 This research was funded by a Discovery Grant to N Ramankutty from the Natural Science and
793 Engineering Research Council (NSERC) of Canada.

794

795 **References**

- 796 Alted, F. & Vilata, I. (2002--). *PyTables: Hierarchical datasets in Python*.
797 <http://www.pytables.org>.
- 798 Barrett, C.B., Barbier, E.B., & Reardon, T. (2001). Agroindustrialization, globalization, and
799 international development: environment implications. *Environment and Development*
800 *Economics*, 419—433.
- 801 Berduegué, J.A. & Fuentealba, R. (2011). Latin America: The state of smallholders in agriculture.
802 *IFAD Conference on New Directions for Smallholder Agriculture, Rome, Italy, Vol. 24*.
- 803 Breiman, L. (2001). Random Forests. *Machine Learning* 45, 5—32.
- 804 Deininger, K., Byerlee, D. (2012). The rise of large farms in land abundant countries: Do they
805 have a future? *World Development* 40, 701—714.
- 806 Dros, J.M. (2004). Managing the soy boom: Two scenarios of soy production expansion in South
807 America. *Amsterdam: AIDEnvironment*.
- 808 Fahrig, L., Girard, J., Duro, D., Pasher, J., Smith, A., Javorek, S., King, D., Lindsay, K.F., Mitchell, S.,
809 & Tischendorf, L. (2015). Farmlands with smaller crop fields have higher within-field
810 biodiversity. *Agriculture, Ecosystems and Environment*, 200, 219—234.
- 811 FAO (Food and Agriculture Organization). (2015). FAOSTAT. <http://faostat.fao.org>.
- 812 Flood, N., Danaher, T., Gill, T., & Gillingham, S. (2013). An operational scheme for standardised
813 surface reflectance from Landsat TM/ETM+ and SPOT HRG imagery for Eastern Australia.
814 *Remote Sensing*, 5, 83—109.
- 815 Foley, J.A., DeFries, R., Asner, G.P., Barford, C., Bonan, G., Carpentar, S.R., Chapin, F.S., Coe,
816 M.T., Daily, G.C., Gibbs, H.K., Helkowski, J.H., Holloway, T., Howard, E.A., Kucharik, C.J.,

817 Monfreda, C., Patz, J.A., Prentice, I.C., Ramankutty, N., & Snyder, P.K. (2005). Global
818 consequences of land use. *Science*, 309, 570—574.

819 Foody, G.M. (2005). Local characterization of thematic classification accuracy through spatially
820 constrained confusion matrices. *International Journal of Remote Sensing*, 26:6, 1217—
821 1228.

822 Fritz, S., See, L., You, L., Justice, C., Becker-Reshef, I., Bydekerke, L., Cumani, R., Defourny, P.,
823 Erb, K., Foley, J., Gilliams, S., Gong, P., Hansen, M., Hertel, T., Herold, M., Herrero, M.,
824 Kayitakire, F., Latham, J., Leo, O., McCallum, I., Obersteiner, M., Ramankutty, N., Rocha, J.,
825 Tang, H., Thornton, P., Vancutsem, C., van der Velde, M., Wood, S., & Woodcock, C.
826 (2013). The need for improved maps of global cropland. *Eos, Transactions, American*
827 *Geophysical Union*, 94(3), 31—32.

828 Fritz, S., See, L., McCallum, I., You, L., Bun, A., Moltchanova, E., Duerauer, M., Albrecht, F., Schill,
829 C., Perger, C., Havlik, P., Mosnier, A., Thornton, Ph., Wood-Sichra, U., Herrero, M., Becker-
830 Reshef, I., Justice, C., Hansen, M., Gong, P., Abdel Aziz, S., Cipriani, A., Cumani, R., Cecchi,
831 G., Conchedda, G., Ferreira, S., Gomez, A., Haffani, M., Kayitakire, F., Malanding, J.,
832 Mueller, R., Newby, T., Nonguierma, A., Olusegun, A., Ortner, S., Ram Rajak, D., Rocha, J.,
833 Schepaschenko, D., Schepaschenko, M., Terekhov, A., Tiangwa, A., Vancutsem, C.,
834 Vintrou, E., Wenbin, W., Van der Velde, M., Dunwoody, A., Kraxner, F., & Obersteiner, M.
835 (2015). Mapping global cropland and field size. *Global Change Biology*, 21, 1980—1992.

836 Gao, F., Masek, J. G., Wolfe, R. E., & Huang, C. (2011). Building a consistent medium resolution
837 satellite data set using moderate resolution imaging spectroradiometer products as
838 reference. *Journal of Applied Remote Sensing*, 4, 043526.

839 Gebhardt, S., Wehrmann, T., Ruiz, M. A. M., Maeda, P., Bishop, J., Schramm, M., Kopeinig, R.,
840 Cartus, O., Kelldorfer, J., Ressler, R., Santos, L. A., & Schmidt, M. (2014). MAD-MEX:
841 Automatic wall-to-wall land cover monitoring for the Mexican REDD-MRV program using
842 all Landsat data. *Remote Sensing*, 6, 3923—3943.

843 Geurts, P., Ernst, D., & Wehenkel, L. (2006). Extremely randomized trees. *Machine Learning*, 63,
844 3—42.

845 Gibbs, H.K., Ruesch, A.S., Achard, F., Clayton, M.K., Holmgren, P., Ramankutty, N., & Foley, J.A.
846 (2010). Tropical forests were the primary sources of new agricultural land in the 1980s
847 and 1990s. *Proceedings of the National Academy of Sciences of the United States of*
848 *America*, 107(38), 16732—16737.

849 Gibbs, H.K., Rausch, L., Munger, J., Schelly, I., Morton, D.C., Noojipady, P., Soares-Filho, B.,
850 Barreto, P., Micol, L., & Walker, N.F. (2015). Brazil's soy moratorium. *Science*, 347(6220),
851 377—378.

852 Gitelson, A.A., Kaufman, Y.J., & Merzlyak, M.N. (1996). Use of a green channel in remote
853 sensing of global vegetation from EOS-MODIS. *Remote Sensing of Environment*, 58(3),
854 289—298.

855 Graesser J., Aide, T.M., Grau, H.R., & Ramankutty, N. (2015). Cropland/pastureland dynamics
856 and the slowdown of deforestation in Latin America. *Environmental Research Letters*, 10,
857 034017.

858 Griffiths, P., van der Linden, S., Kuemmerle, T., & Hostert, P. (2013). A pixel-based Landsat
859 compositing algorithm for large area land cover mapping. *IEEE Journal of Selected Topics*
860 *in Applied Earth Observations and Remote Sensing*, 6(5), 2088—2101.

861 Guizar-Sicairos, M., Thurman, S.T., Fienup, J.R. (2008). Efficient subpixel image registration
862 algorithms. *Optics Letters*, 33(2), 156—158.

863 Hansen, M.C., Roy, D.P., Lindquist, E., Adusei, B., Justice, C. O., & Altstatt, A. (2008). A method
864 for integrating MODIS and Landsat data for systematic monitoring of forest cover and
865 change in the Congo Basin. *Remote Sensing of Environment*, 112, 2495—2513.

866 Hansen, M.C., Loveland, T.R. (2012). A review of large area monitoring of land cover change
867 using Landsat data. *Remote Sensing of Environment*, 122, 66—74.

868 Hansen, M.C., Potapov, P.V., Moore, R., Hancher, M., Turubanova, S.A., Tyukavina, A., Thau, D.,
869 Stehman, S.V., Goetz, S.J., Loveland, T.R., Kommareddy, A., Egorov, A., Chini, L., Justice,
870 C.O., Townshend, J.R.G. (2013). High-resolution global maps of 21st-century forest change.
871 *Science*, 342, 850—853.

872 Hermosilla, T., Wulder, M.A., White, J.C., Coops, N.C., Hobart, G.W. (2015). An integrated
873 Landsat time series protocol for change detection and generation of annual gap-free
874 surface reflectance composites. *Remote Sensing of Environment*, 158, 220—234.

875 Jiang, Zhangyan, Huete, Alfredo R., Didan, Kamel, & Miura, Tomoaki. (2008). Development of a
876 two-band enhanced vegetation index without a blue band. *Remote Sensing of*
877 *Environment*, 112, 3833—3845.

878 Kuemmerle, T., Hostert, P., St-Louis, V., & Radeloff, V. C. (2009). Using image texture to map
879 farmland field size: a case study in Eastern Europe. *Journal of Land Use Science*, 4(1-2),
880 85—107.

881 Kuemmerle, T., Erb, K., Meyfroidt, P., Müller, D., Verburg, P. H., Estel, S., Haberl, H., Hostert, P.,
882 Jepsen, M. R., Kastner, T., Levers, C., Lindner, M., Plutzar, C., Verkerk, P. J., van der

883 Zanden, E., H., Reenberg, A. (2013). Challenges and opportunities in mapping land use
 884 intensity globally. *Current Opinion in Environmental Sustainability*, 5(1), 1—10.

885 Kovalskyy, V. & Roy, D.P. (2013). The global availability of Landsat 5 TM and Landsat 7 ETM+
 886 land surface observations and implications for global 30 m Landsat data product
 887 generation. *Remote Sensing of Environment*, 130, 280—293.

888 Lam, L., Seong-Whan, L., Suen, C.Y. (1992). Thinning methodologies—A comprehensive survey.
 889 *IEEE Transactions on Pattern Analysis and Machine Intelligence*, 14(9), 869—885.

890 Liu, H. & Setiono, R. (1995). Chi2: feature selection and discretization of numeric attributes. In
 891 the *Proceedings of the 7th International Conference on Tools with Artificial Intelligence*,
 892 (Nov), 388—391.

893 Lorenz, M.O. (1905). Methods of measuring the concentration of wealth. *Publications of the*
 894 *American statistical association*, 9(70), 209—219.

895 Martinelli, L.A. (2012). Ecosystem services and agricultural production in Latin America and the
 896 Caribbean. *Inter-American Development Bank*.

897 Maxwell, S. K. & Sylvester, K. M. (2012). Identification of “ever-cropped” land (1984-2010) using
 898 Landsat annual maximum NDVI image composites: Southwestern Kansas case study.
 899 *Remote Sensing of Environment*, 121, 186—195.

900 Matson, P.A., Parton, W.J., Power, A.G., Swift, M.J. (1997). Agricultural intensification and
 901 ecosystem properties. *Science*, 277, 504—509.

902 Olofsson, P., Foody, G. M., Stehman, S. V., & Woodcock, C. E. (2013). Making better use of
 903 accuracy data in land change studies: Estimating accuracy and area and quantifying
 904 uncertainty using stratified estimation. *Remote Sensing of Environment*, 129, 122—131.

905 Olson, D. M., Dinerstein, E., Wikramanayake, E. D., Burgess, N. D., Powell, G. V. N., Underwood,
 906 E. C., D'amico, J. A., Itoua, I., Strand, H. E., Morrison, J. C., Loucks, C. J., Allnutt, T. F.,
 907 Ricketts, T. H., Kura, Yumiko, Lamoreux, J. F., Wettengel, W. W., Hedao, P., & Kassem, K.
 908 R. (2001). Terrestrial ecoregions of the world: a new map of life. *BioScience*, 51, 933—938.

909 Pedregosa, F., Varoquaux, G., Gramfort, A., Michel, V., Thirion, B., Grisel, O., Blondel, M.,
 910 Prettenhofer, P., Weiss, R., Dubourg, V., Vanderplas, J., Passos, A., Cournapeau, D.,
 911 Brucher, M., Perrot, M., & Duchesnay, E. (2011). Scikit-learn: Machine learning in Python.
 912 *Journal of Machine Learning Research*, 12, 2825—2830.

913 Persello C. & Bruzzone, L. (2010). A novel protocol for accuracy assessment in classification of
 914 very high resolution images. *IEEE Transactions on Geoscience and Remote Sensing*, 48:3,
 915 1232—1244.

916 Potapov, P. V., Turubanova, S. A., Hansen, M. C., Adusei, B., Broich, M., Altstatt, A., Mane, L., &
 917 Justice, C. O. (2012). Quantifying forest cover loss in Democratic Republic of the Congo,
 918 2000-2010, with Landsat ETM+ data. *Remote Sensing of Environment*, 122, 106—116.

919 Rogers, A. S. & Kearney, M. S. (2004) Reducing signature variability in unmixing coastal marsh
 920 Thematic Mapper scenes using spectral indices. *International Journal of Remote Sensing*,
 921 25(12), 2317—2335.

922 Roy, D. P., Ju, J., Kline, K., Scaramuzza, P. L., Kovalsky, V., Hansen, M., Loveland, T. R., Vermote,
 923 E., & Zhang, C. (2010). Web-enabled Landsat data (WELD): Landsat ETM+ composited
 924 mosaics of the conterminous United States. *Remote Sensing of Environment*, 114, 35—49.

925 Savitsky, A. & Golay, M.J.E. (1964). Smoothing and differentiation of data by simplified least
 926 squares procedures. *Analytical Chemistry*, 36(8), 1627—1639.

927 Schmidt, M., Pringle, M., Devadas, R. Denham, R. & Tindall, D. (2016). A framework for large-
 928 area mapping of past and present cropping activity using seasonal Landsat images and
 929 time series metrics. *Remote Sensing*, 8(312), 1—25.

930 Theil, H. (1992). *A rank-invariant method of linear and polynomial regression analysis*. Henri
 931 Theil's contributions to economics and econometrics (Springer), 345—381.

932 Tilman, D., Farigione, J., Wolff, B., D'Antonio, C., Dobson, A., Howarth, R., Schindler, D.,
 933 Schlesinger, W.H., Simberloff, D., Swackhamer, D. (2001). Forecasting agriculturally driven
 934 environmental change. *Science*, 292, 281—284.

935 Tilman, D., Cassman, K. G., Matson, P. A., Naylor, R., & Polasky, S. (2002). Agricultural
 936 sustainability and intensive production practices. *Nature*, 418.

937 Tomasi, C. & Manduchi, R. (1998). Bilateral filtering for gray and color images. *Proceedings of*
 938 *the Sixth IEEE International Conference on Computer Vision, Bombay, India*, 839—846.

939 Toivonen, T., Kalliola, R., Ruokolainen, K., & Malik, R. N. (2006). Across-path DN gradient in
 940 Landsat TM imagery of Amazonian forests: A challenge for image interpretation and
 941 mosaicking. *Remote Sensing of Environment*, 100(4), 550—562.

942 Tucker, C. J. (1979). Red and photographic red linear combinations for monitoring vegetation.
 943 *Remote Sensing of Environment*, 8, 127—150.

944 USGS (2004) SLC-off gap-filled products gap-fill algorithm methodology: Phase2 gap-fill al-
 945 gorithm (<http://landsat.usgs.gov>).

946 Vallejos, M., Volante, J. N., Mosciaro, M. J., Vale, L. M., Bustamante, M. L., & Paruelo, J. M.
 947 (2015). Transformation dynamics of the natural cover in the Dry Chaco ecoregion: A plot
 948 level geo-database from 1976 to 2012. *Journal of Arid Environments*, 123, 3—11.

949 Vermote, E. F., Tanré, D., Deuzé, J. L., Herman, M., & Morcrette, J.-J. (1997). Second simulation
 950 of the satellite signal in the solar spectrum, 6S: an overview. *IEEE Transactions on*
 951 *Geoscience and Remote Sensing*, 35(3), 675—686.

952 Weissteiner, C. J., García-Feced, C., Paracchini, M. L. (2016). A new view on EU agricultural
 953 landscapes: Quantifying patchiness to assess farmland heterogeneity. *Ecological*
 954 *Indicators*, 61, 317—327.

955 White, J.C., Wulder, M.A., Hobart, G.W., Luther, J.E., Hermosilla, T., Griffiths, P., Coops, N.C.,
 956 Hall, R.J., Hostert, P., Dyk, A., & Guindon, L. (2014). Pixel-based image compositing for
 957 large-area dense time series applications and science. *Canadian Journal of Remote*
 958 *Sensing*, 40(3), 192—212.

959 Whiteside T.G., Maier S.W., & Boggs G.S. (2014). Area-based and location-based validation of
 960 classified image objects. *International Journal of Applied Earth Observation and*
 961 *Geoinformation*, 28, 117—130.

962 Woodcock, C.E., Allen, A.A., Anderson, M., Belward, A.S., Bindschadler, R., Cohen, W.B., Gao, F.,
 963 Goward, S.N., Helder, D., Helmer, E., Nemani, R., Oreopoulos, L., Schott, J., Thenkabail,
 964 P.S., Vermote, E.F., Vogelmann, J., Wulder, M.A., & Wynne, R. (2008). Free access to
 965 Landsat imagery. *Science*, 320, 1011.

966 Yan, L. & Roy, D. P. (2014). Automated crop field extraction from multi-temporal Web Enabled
 967 Landsat Data. *Remote Sensing of Environment*, 144, 42—64.

968 Yan, L. & Roy, D. P. (2016). Conterminous United States crop field size quantification from
 969 multi-temporal Landsat data. *Remote Sensing of Environment*, 172, 67—86.

- 970 Zhao, H. & Chen, X. (2005). Use of normalized difference bareness index in quickly mapping
971 bare areas from TM/ETM+. *Proceedings of the 2005 IEEE Geoscience and Remote Sensing*
972 *Symposium*.
- 973 Zhang, T.Y. & Suen, C.Y. (1984). A fast parallel algorithm for thinning digital patterns. *Image*
974 *Processing and Computer Vision*, 27(3), 236—239.
- 975 Zhang, C., Li, W., & Travis D. (2007). Gaps-fill of SLC-off Landsat ETM+ satellite image using a
976 geostatistical approach. *International Journal of Remote Sensing*, 28(22), 5103—5122.
- 977 Zhu, Z. & Woodcock, C. E. (2012). Object-based cloud and cloud shadow detection in Landsat
978 imagery. *Remote Sensing of Environment*, 118, 83—94.
- 979 Zuiderveld, K. (1994). Contrast limited adaptive histogram equalization. *Graphics gems IV*,
980 Academic Press Professional, Inc., 474—485.